
# Characteristics of Lake-Effect Precipitation over the Black River Valley and Western Adirondack Mountains

W. JAMES STEENBURGH,[a] JULIE A. CUNNINGHAM,[a,b] PHILIP T. BERGMAIER,[c] BART GEERTS,[d] AND PETER VEALS[a]

[a] *Department of Atmospheric Sciences, University of Utah, Salt Lake City, Utah*
[b] *NOAA/National Weather Service Forecast Office, Salt Lake City, Utah*
[c] *Wyoming NASA Space Grant Consortium, University of Wyoming, Laramie, Wyoming*
[d] *Department of Atmospheric Science, University of Wyoming, Laramie, Wyoming*

(Manuscript received 12 February 2023, in final form 27 July 2023, accepted 29 July 2023)

ABSTRACT: Potential factors affecting the inland penetration and orographic modulation of lake-effect precipitation east of Lake Ontario include the environmental (lake, land, and atmospheric) conditions, mode of the lake-effect system, and orographic processes associated with flow across the downstream Tug Hill Plateau (herein Tug Hill), Black River valley, and Adirondack Mountains (herein Adirondacks). In this study we use data from the KTYX WSR-88D, ERA5 reanalysis, New York State Mesonet, and Ontario Winter Lake-effect Systems (OWLeS) field campaign to examine how these factors influence lake-effect characteristics with emphasis on the region downstream of Tug Hill. During an eight-cool-season (16 November–15 April) study period (2012/13–2019/20), total radar-estimated precipitation during lake-effect periods increased gradually from Lake Ontario to upper Tug Hill and decreased abruptly where the Tug Hill escarpment drops into the Black River valley. The axis of maximum precipitation shifted poleward across the northern Black River valley and into the northwestern Adirondacks. In the western Adirondacks, the heaviest lake-effect snowfall periods featured strong, near-zonal boundary layer flow, a deep boundary layer, and a single precipitation band aligned along the long-lake axis. Airborne profiling radar observations collected during OWLeS IOP10 revealed precipitation enhancement over Tug Hill, spillover and shadowing in the Black River valley where a resonant lee wave was present, and precipitation invigoration over the western Adirondacks. These results illustrate the orographic modulation of inland-penetrating lake-effect systems downstream of Lake Ontario and the factors favoring heavy snowfall over the western Adirondacks.

SIGNIFICANCE STATEMENT: Inland penetrating lake-effect storms east of Lake Ontario affect remote rural communities, enable a regional winter-sports economy, and contribute to a snowpack that contributes to runoff and flooding during thaws and rain-on-snow events. In this study we illustrate how the region's three major geographic features—Tug Hill, the Black River valley, and the western Adirondacks—affect the characteristics of lake-effect precipitation, describe the factors contributing to heavy snowfall over the western Adirondacks, and provide an examples of terrain effects in a lake-effect storm observed with a specially instrumented research aircraft.

KEYWORDS: Lake effects; Snowfall; Orographic effects

## 1. Introduction

Lake-effect snowstorms that develop during cold-air outbreaks over warm bodies of water often produce heavy localized snowfall that can paralyze downstream communities. Accurate prediction of these snowstorms is crucial for protecting life and property and minimizing transportation and other disruptions (e.g., Schmidlin 1993; Niziol et al. 1995; Fujisaki-Manome et al. 2022). Snowbelts climatologically downstream of the Great Lakes of North America receive plentiful lake-effect snow each year (e.g., Muller 1966; Norton and Bolsenga 1993; Niziol et al. 1995; Jones et al. 2022). East of Lake Ontario, the Tug Hill Plateau (herein Tug Hill) averages over 500 cm (200 in.) of snow annually, a result of frequent lake-effect snowstorms and local enhancement processes due to coastal and orographic effects (e.g., Minder et al. 2015; Veals and Steenburgh 2015; Campbell and Steenburgh 2017; Steenburgh and Campbell 2017; Veals et al. 2018). During thaws and rain-on-snow events, the melting of lake-effect snow contributes to flooding that can be exacerbated by frozen soils, which prevent groundwater infiltration, and ice flows or jams (Langbein et al. 1947; Hoyt and Langbein 1955). Although prior studies noted above have examined precipitation

*Corresponding author*: Jim Steenburgh, jim.steenburgh@utah.edu

DOI: 10.1175/JAMC-D-23-0026.1

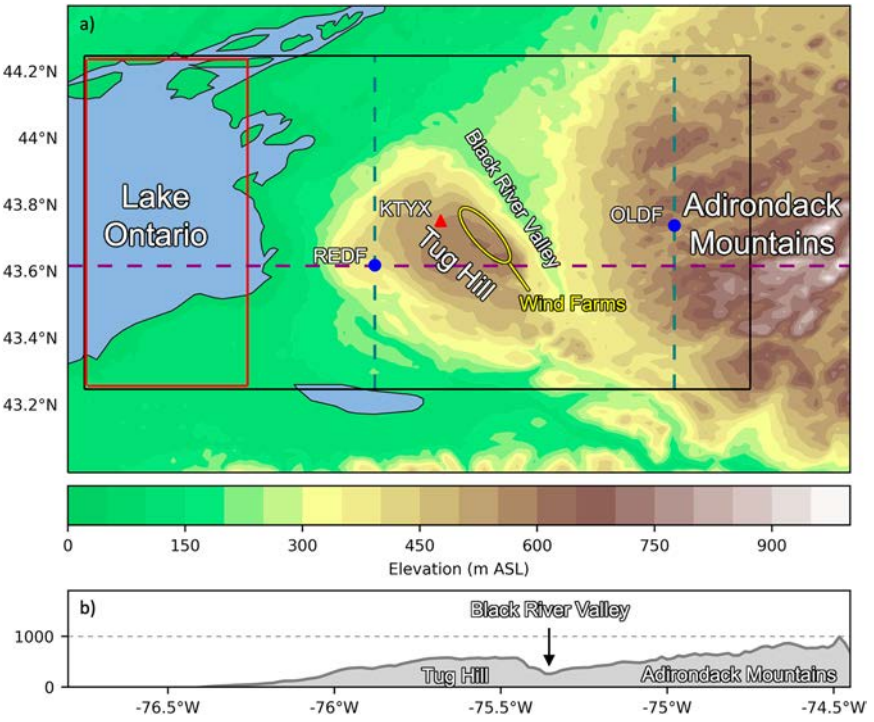


FIG. 1. (a) Geography and topography (m MSL) of the study region with the REDF and OLDF New York State Mesonet sites identified with blue dots and the KTYX WSR-88D shown with a red triangle. Maple Ridge and Madison Wind Farms are outlined with a yellow oval. Black- and red-outlined rectangles define the averaging areas for ERA5 variables. Dashed teal lines indicate REDF and OLDF meridians. (b) Topography (m MSL) along a zonal transect [43.62°N; dashed maroon line in (a)].

enhancement over Tug Hill, lake-effect systems often extend farther inland across the Black River valley (BRV) and the western Adirondack Mountains (herein Adirondacks), affecting rural communities and winter recreation.

Lake-effect snowstorms are generated during cold-air outbreaks as sensible and latent heat fluxes from the warmer lake surface warm, moisten, destabilize, and deepen the convective boundary layer (CBL), leading to the development of moist convection (e.g., Peace and Sykes 1966; Hjelmfelt and Braham 1983; Niziol et al. 1995). Many factors influence the characteristics of lake-effect storms. Larger lake-air temperature differences, stronger winds, and a longer fetch produce a deeper CBL that enables stronger convection and greater liquid equivalent precipitation (e.g., Hill 1971; Braham 1983; Niziol 1987; Hjelmfelt 1990; Byrd et al. 1991; Kristovich et al. 1999; Laird and Kristovich 2002). Event characteristics are also affected by the mode of the lake-effect system, which includes broad-coverage convection (typically open cellular or wind-parallel bands), or long-lake-axis parallel (LLAP) bands generated by land-breeze convergence (e.g., Peace and Sykes 1966; Passarelli and Braham 1981; Kelly 1982, 1984, 1986; Braham 1983; Kristovich 1993; Laird and Kristovich 2004; Steiger et al. 2013; Steenburgh and Campbell 2017). Broad coverage periods typically are associated with weaker precipitation rates, whereas LLAP bands produce more localized but intense snowfall rates. Additional lake-effect modes identified over and downstream of Lake Ontario include hybrids of broad coverage and LLAP band systems, shoreline bands, mesoscale vortices, and lake-orographic systems with a stationary precipitation region over downstream orography (Veals and Steenburgh 2015).

Tug Hill is the first major topographic feature encountered by lake-effect systems east of Lake Ontario and rises gradually to an elevation of about 500 m above lake level (Figs. 1a,b). Mean cool-season lake-effect precipitation maximizes over the western and upper (windward) slopes of Tug Hill, which reflects coastal, orographic, and other influences (Niziol et al. 1995; Veals and Steenburgh 2015; Campbell et al. 2016; Campbell and Steenburgh 2017; Veals et al. 2018; Gowan et al. 2021, 2022). To the east, the Tug Hill escarpment drops into the Black River valley. The terrain then rises gradually into the western Adirondacks to elevations higher than Tug Hill. Lake-effect spillover into the Black River valley and maintenance or invigoration over the western Adirondacks is a critical forecast issue for rural communities and winter recreation in the region. The eastern Tug Hill and western Adirondacks are also the headwaters of the Black River, with half of the annual runoff occurring during the mid-February–mid-May snowmelt season. In addition, rain-on-snow events produce the greatest potential for flooding (Black River Watershed Management Plan 2010).

As a result of the 2013/14 Ontario Winter Lake-effect Systems (OWLeS) field campaign (Kristovich et al. 2017), many recent studies have examined lake-effect systems generated

by Lake Ontario, especially over Tug Hill. Environmental factors that have been linked to the intensity and/or distribution of lake-effect precipitation in this region include the strength of the incident flow, lake-induced convective available potential energy (LCAPE), lake-air temperature difference, differential cold-air advection, multilake connections, and orographic effects (Veals et al. 2018; Villani et al. 2017; Campbell and Steenburgh 2017; Kristovich et al. 2018; Lang et al. 2018; Eipper et al. 2018, 2019). Lake-effect mode also plays a role with well-developed LLAP band periods (herein "banded") producing the highest precipitation rates but small orographic enhancement ratios (i.e., the ratio of upland to lowland precipitation) and nonbanded broad-coverage periods (herein "nonbanded") producing the lowest precipitation rates but the largest orographic enhancement ratios (Campbell et al. 2016; Veals et al. 2018). In addition to orographic processes, ascent along a land-breeze front can contribute to the maximum in lake-effect precipitation over Tug Hill (Campbell and Steenburgh 2017; Steenburgh and Campbell 2017). Although conceptual models often emphasize an invigoration of lake-effect convection over downstream orography, lake-effect systems typically exhibit a convective-to-stratiform transition from Lake Ontario to upper Tug Hill (Minder et al. 2015).

The evolution of lake-effect systems east (downstream) of Tug Hill has not been carefully investigated. In other regions, water-vapor depletion and terrain-induced subsidence can produce precipitation shadowing downstream of hills and mountains, but significant spillover can occur in some situations (Brady and Waldstreicher 2001; Ralph et al. 2003; Siler et al. 2013; Mass et al. 2015; Siler and Durran 2016; Stockham et al. 2018). Mechanisms contributing to spillover include the existence of a lee-side cold pool, which suppresses leeward subsidence, and reduced upstream stability with strong cross-barrier flow, which increases orographic enhancement and spillover distance (e.g., Sinclair et al. 1997; Nakai and Endoh 1995; Chater and Sturman 1998; Siler and Durran 2016). Depending on where potential instability is released on the windward side, convection may also result in proportionally more precipitation in the lee (Zängl 2005; Geerts et al. 2015). Cloud microphysical processes may also play a role, with lower hydrometeor fall speeds resulting in greater downstream hydrometeor transport into the lee (e.g., Chater and Sturman 1998; Roe and Baker 2006; Geerts et al. 2015; Zagrodnik et al. 2021).

Snowfall in the western Adirondacks requires the penetration of lake-effect systems well inland from Lake Ontario and/or invigoration during orographic uplift. Previous studies have identified some of the factors influencing the inland penetration of lake-effect precipitation systems. Eipper et al. (2018) identified statistically significant correlations between inland penetration and two environmental parameters: cold-air advection in the upper portion of the CBL and CBL depth. Cold-air advection in the upper portion of the CBL destabilizes the lower atmosphere and represents an inland power source for continued moist convection. A deeper CBL may indicate greater available moisture and more intense LLAP bands. Eipper et al. (2018) also suggested a linkage between inland penetration and 850-hPa wind speed, although this relationship was not statistically significant. Villani et al. (2017) however, suggested that the mean mixed-layer wind speed is correlated with inland penetration, along with the existence of a multilake/upstream moisture source or connection, a larger lake-air temperature difference, and increased 0–1-km bulk shear.

In the present study, we focus on the characteristics of lake-effect storms downstream of Tug Hill over the Black River valley and western Adirondacks. We aim to elucidate the environmental, morphological, and orographic factors that influence lake-effect precipitation over these inland topographic features. Section 2 describes the datasets and methods used to perform the analysis. Section 3 describes the relationship between key environmental variables and the characteristics of lake-effect precipitation over the Black River valley and western Adirondacks based on radar observations during eight cool seasons. Section 3 also presents airborne profiling radar observations collected during OWLeS IOP10, which provides a unique perspective on the inland penetration and orographic modulation of lake-effect precipitation over these orographic features. The paper concludes with a summary of key findings in section 4.

## 2. Data and methods

### a. Event and morphology identification

Level-II radar observations from the Montague/Fort Drum, New York (KTYX), WSR-88D, located at 562 m MSL on Tug Hill, were downloaded from the National Centers for Environmental Information (NCEI) and used to identify and examine the characteristics of lake-effect storms across Tug Hill, the Black River valley, and western Adirondacks. Lake-effect periods come in part from the climatologies developed by Veals and Steenburgh (2015) and Veals et al. (2018), which spanned nine cool seasons (16 November–15 April) from November 2008 to April 2017. We focused, however, on events beginning in the 2012/13 cool season to enable the use of dual-polarization (dual-pol) products for radar processing and identified additional cases as described in Veals and Steenburgh (2015) through the 2019/20 season. Thus, our climatology covers eight cool seasons from 2012/13 to 2019/20. One exception is the analysis in which we examine how the lake-effect morphology (i.e., banded or nonbanded) affects western Adirondack precipitation. This is based on a subset of cases from Veals et al. (2018) during the 2012/13–2016/17 cool seasons in which the morphology of the lake-effect precipitation features was identified in 3-h intervals along a transect at 43.62°N (Figs. 1a,b).

### b. Radar estimated precipitation and quality control

Following Campbell et al. (2016), we estimated liquid precipitation equivalent (LPE) during these lake-effect periods using the $Z$–$S$ relationship described by Vasiloff (2001):

$$Z = 75S^2, \tag{1}$$

where $Z$ is the lowest-level (0.5°) radar reflectivity factor ($mm^6\ m^{-3}$), and $S$ is the LPE rate ($mm\ h^{-1}$). Three-hourly radar-estimated precipitation (REP) was derived by integrating the LPE rate for each lowest-level scan over a 3-h period.

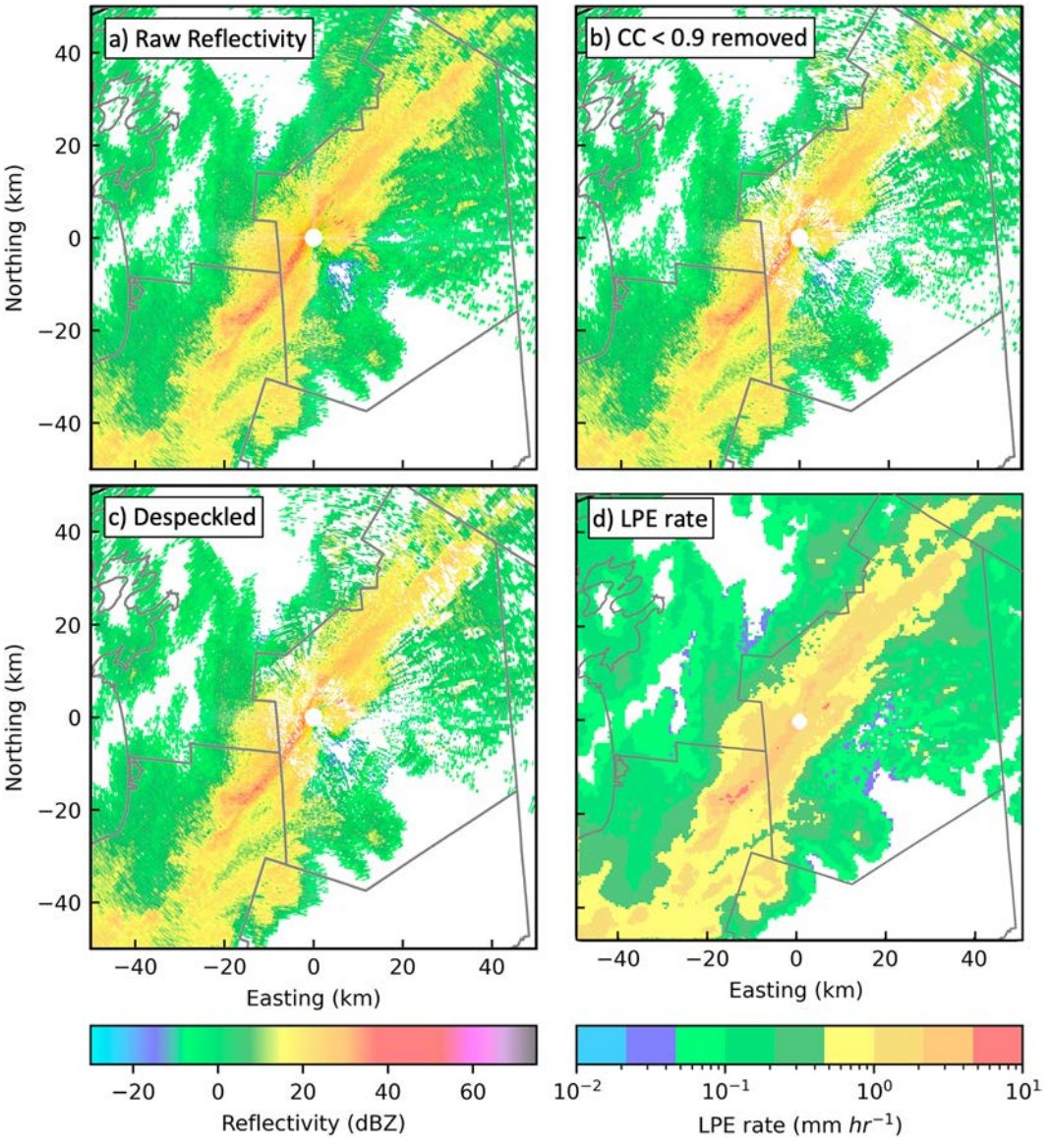


FIG. 2. Radar quality control and estimated precipitation: (a) raw reflectivity (dB$Z$), (b) reflectivity (dB$Z$) after removing gates with correlation coefficient $< 0.9$, (c) reflectivity (dB$Z$) after application of the Py-Art despeckling algorithm, and (d) LPE rate (mm h$^{-1}$) after conversion to Cartesian coordinate system and application of the $Z$–$S$ relationship.

A major challenge for precipitation estimates in the study region is wind turbine clutter (WTC) from the Maple Ridge and Madison Wind Farms on upper Tug Hill (Fig. 1a). Not only is there clutter produced locally by the turbines, but there is also multipath scattering as far as 50 km down radial (Radar Operations Center 2022). Although radar clutter often has zero or near-zero Doppler velocity, the wind turbines move and frequently have a nonzero velocity, complicating clutter removal (Norin and Haase 2012; Radar Operations Center 2022). The multipath scattering also varies temporally and must be removed scan by scan rather than using static maps.

Multiple approaches have been proposed to filter wind-turbine effects from radar data (see section 3.1.3 of Norin and Haase 2012). We used a simple but straightforward approach that reduces these artifacts, especially multipath scattering, although some artifacts remain, especially in the Maple Ridge Wind Farm area. We began with the lowest-tilt reflectivity data (Fig. 2a) and removed all range gates with a correlation coefficient $< 0.9$ (Fig. 2b), which typically reflects nonmeteorological targets (Zrnić et al. 2006; Frech and Seltmann 2017). We then used the Py-Art despeckling algorithm (Helmus and Collis 2016) to remove extraneous clusters of radar echoes covering an area smaller than 20 range gates (Fig. 2c; changes most apparent

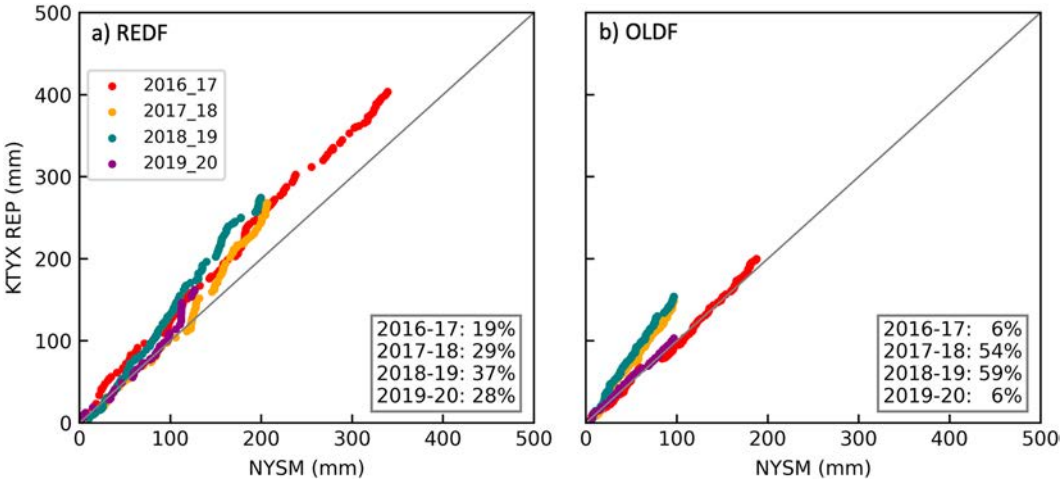


FIG. 3. Comparison of a 3-h running accumulation of KTYX REP (mm) with NYSM LPE (mm) during lake-effect periods at (a) REDF and (b) OLDF. Inset boxes indicate the REP overestimation in each cool season.

near 0 northing between −50 and −20 easting). These clusters often resulted from multipath scattering down radial of wind turbines, including outside the area of lake-effect precipitation. We then filled the removed gates in contiguous precipitation areas using nearest neighbor interpolation, converted from antenna to cartesian coordinates at 500-m horizontal grid spacing, and applied the $Z$–$S$ relationship (Fig. 2d). This reduces many of the issues with multipath scattering, but some artifacts remain, especially in the wind-farm area where time-averaged LPE rates may be anomalously high due to the intermittent presence of clutter.

Assuming standard atmospheric refraction, the centroid of the lowest-level (0.5°) scan is generally above the topography (Brown et al. 2007), but there are sometimes terrain-blocked radials in the vicinity of the ~135° and ~340° azimuths (Veals and Steenburgh 2015). The effects of the latter are minimal, but the former is evident in the radar statistics as no attempt was made to fill this region. The effects of any ground clutter not accounted for by the approaches described above to deal with wind turbine clutter appeared to be minimal. Additionally, by focusing on lake-effect periods from 16 November to 15 April, we minimize the influence of lake-effect rain events that could include a radar bright band.

### c. Validation

To test the validity of these quality control and precipitation estimation methods, we compared the REP with LPE measurements from six New York State Mesonet sites that began operating prior to the 2016/17 cool season. These sites provide LPE measurements every 5 min using an OTT Pluvio$^2$ 200 weighing gauge that includes a heated rim to prevent snow and ice buildup and a proprietary algorithm to adjust for wind and temperature effects (Brotzge et al. 2020). A double Alter wind shield surrounds the gauge to reduce the undercatch of frozen precipitation. For comparison, the REP is averaged over a 9-gridpoint (3 × 3) stencil centered on each observing site.

Results were generally consistent across all six sites, so for brevity, we present a comparison of REP and measured LPE during lake-effect periods at the Redfield (REDF) and Old Forge (OLDF) sites on the western (windward) slopes of Tug Hill and the Adirondacks, respectively, which is the focus region of our analysis (Fig. 3). At REDF, the REP is 27% higher than observed with a range of 19%–37% by cool season. At OLDF, the REP is also 27% higher, with a range of 6%–60% by cool season. These values are somewhat higher than the 10% and 15% REP overestimation relative to manual snow samples at Redfield and Sandy Creek during the OWLeS field program (Veals et al. 2018), possibly due to an inability of the proprietary algorithms to fully account for gauge undercatch. These values also suggest that the REP is within the undercatch uncertainty exhibited by precipitation gauges, even when undercatch algorithms are applied (Rasmussen et al. 2012; Pierre et al. 2019). Thus, we have not attempted to refine the $Z$–$S$ relationship but suggest that our estimates may be slightly higher than actual values.

### d. Environmental conditions

We examined the relationship between several environmental variables and lake-effect precipitation east of Tug Hill and over the western Adirondacks. These variables were obtained or derived from the ERA5 Reanalysis (Hersbach et al. 2020), which was downloaded from the Copernicus Climate Change Service (CS3) Climate Data Store (https://cds.climate.copernicus.eu/#!/home) at 0.25° horizontal grid spacing, 25-hPa vertical grid spacing at and below 750 hPa, 50-hPa vertical grid spacing above 750 hPa, and hourly intervals. The hourly data were averaged into 3-h intervals and spatially averaged over the region in the black or red rectangles in Fig. 1a, depending on the variable. The black rectangle covers the region over and immediately inland from Lake Ontario, whereas the red rectangle covers eastern Lake Ontario.

Mean boundary layer zonal wind speed $\overline{U}$ has been shown to influence the intensity and distribution of lake-effect

precipitation. Following Veals et al. (2018), $\overline{U}$ was based on the mean zonal wind in the 850–950-hPa layer and averaged over the black rectangle. We also examined mean boundary layer wind direction, similarly based on the mean wind in the 850–950-hPa layer and averaged over the black-outlined rectangle, which was previously examined in Veals and Steenburgh (2015) for lake-effect precipitation on the windward side of Tug Hill. Boundary layer depth was obtained from the ERA5 and averaged over the red-outlined rectangle. LCAPE provides an estimate of the instability of the lake-effect environment (e.g., Niziol 1987; Steiger et al. 2009; Veals et al. 2018) and was calculated using the MetPy Python library (May et al. 2022) cape_cin calculation function using ERA5 pressure level data aloft and the lake-surface temperature as the surface temperature and dewpoint, assuming a surface pressure of 1004 hPa. The ERA5 pressure level data and lake-surface temperatures were averaged over the red rectangle for the LCAPE calculation.

### e. Environmental diagnostics

To examine the relationship between the environmental variables described above and western Adirondack precipitation, we identified the maximum precipitation rate for each 3-h period along the meridian corresponding to the OLDF New York State Mesonet site (Fig. 1a). In addition to being a New York State Mesonet Site, OLDF is a winter-recreation center located within the snowiest area of the western Adirondacks (National Weather Service 2022; Steenburgh 2023, his Fig. 3.10). We then defined high precipitation (HP) periods as those when the precipitation rate was in the upper quintile of all 3-h lake-effect periods, which yielded 434 HP and 1750 non-HP periods, with HP periods most common in December and January, similar to lake-effect periods in general (Veals and Steenburgh 2015). The upper quintile threshold was 1.8 mm $(3\ \text{h})^{-1}$. Assuming a climatological snow-to-liquid ratio of 14 to 1 (Baxter et al. 2005) a 3-h accumulation of 1.8 mm corresponds to a snowfall rate of 2.5 cm $(3\ \text{h})^{-1}$. In our analysis, we compared the distributions of each environmental variable during HP periods with all other periods, which we labeled as non-HP periods, and examined precipitation characteristics during periods in the upper quintile (high), middle quintile (medium), and lower quintile (low) of the distribution of each variable.

### f. Airborne radar data

Detailed airborne profiling radar observations of banded lake-effect precipitation and its inland penetration over the Tug Hill and the western Adirondacks were obtained during OWLeS intensive observing period 10 (IOP10) by the University of Wyoming King Air (UWKA). During IOP10, the UWKA was equipped with instruments to measure basic meteorological variables as well as the Wyoming Cloud Radar (WCR), a 95-GHz Doppler radar (Kristovich et al. 2017). Radar reflectivity and Doppler velocity measurements were sampled every 4–5 m along the flight track and in range increments of 15 m for three fixed antennas: one pointing up (near zenith), one pointing down (near nadir), and one pointing down-forward (~30° forward of nadir). The first two provide a vertical profile from cloud top to the ground, whereas the two downward-pointing antennas provide the along-track horizontal and vertical velocities through dual-Doppler synthesis. We focus on the sole along-wind flight leg flown during IOP10 from the central Adirondacks westward over the Black River valley and Tug Hill to the eastern end of Lake Ontario.

Bergmaier et al. (2017) describe the WCR Doppler data processing method. Horizontal wind profiles from proximity soundings collected from North Redfield on Tug Hill during the UWKA flight described herein[1] were used to remove the horizontal wind contribution from the zenith and nadir beam Doppler velocities when the beams were not oriented vertically due to aircraft attitude variations. Furthermore, WCR reflectivity-weighted hydrometeor vertical velocity $w_H$ measurements from the zenith and nadir beams were used to retrieve the air vertical velocity. We used a method described by Zaremba et al. (2022), which assumes that the mesoscale (leg mean) air vertical velocity is zero over the length of the full flight track, and subtracts the flight-leg-mean hydrometeor fall speed (or terminal velocity $V_t$, which is positive downward) at each height level, to obtain the best-guess air vertical velocity $w = w_H - V_t$. The assumption of zero mean air vertical velocity (i.e., the magnitude of updrafts and downdrafts average to zero at each height level) is appropriate for sufficiently long flight legs, such as the >100-km-long leg used here given the uncertainty of the Doppler radar measurements. The flight leg was roughly aligned with the prevailing wind, which makes retrieval of dual-Doppler velocities more accurate than for crosswind flight legs (Bergmaier et al. 2017). Along-track horizontal velocities $u$ of hydrometeors from the dual-Doppler synthesis were processed with horizontal-by-vertical grid spacings of $90 \times 60\ \text{m}^2$ and projected onto a straight Cartesian grid aligned with the flight leg. These velocities, together with those obtained from the nadir beam, were used to calculate 2D hydrometeor streamline estimates below flight level. By definition, these streamlines are tangential to the 2D hydrometeor motion vector $(u, w_H)$ at any point in the 2D grid. They can be interpreted as Lagrangian hydrometeor trajectories only if the flow is steady state.

## 3. Results

### a. Climatological characteristics

Over the eight cool seasons, there were 2184 three-hour lake-effect periods totaling 6552 lake-effect hours (a mean of 819 per season). The highest mean monthly frequency of lake-effect hours was in January (622 h), and the lowest was in April (77 h), although events were only identified for the first half of the latter. The number of lake-effect hours per season varied between 453 in 2016/17 and 1005 in 2019/20.

The mean 3-h LPE rate during lake-effect periods increases from eastern Lake Ontario to a maximum over Tug Hill (Fig. 4a), consistent with Veals et al. (2018). The axis of maximum mean

[1] The North Redfield sounding site was ~250 m north of the current REDF New York State Mesonet site identified in Fig. 1.

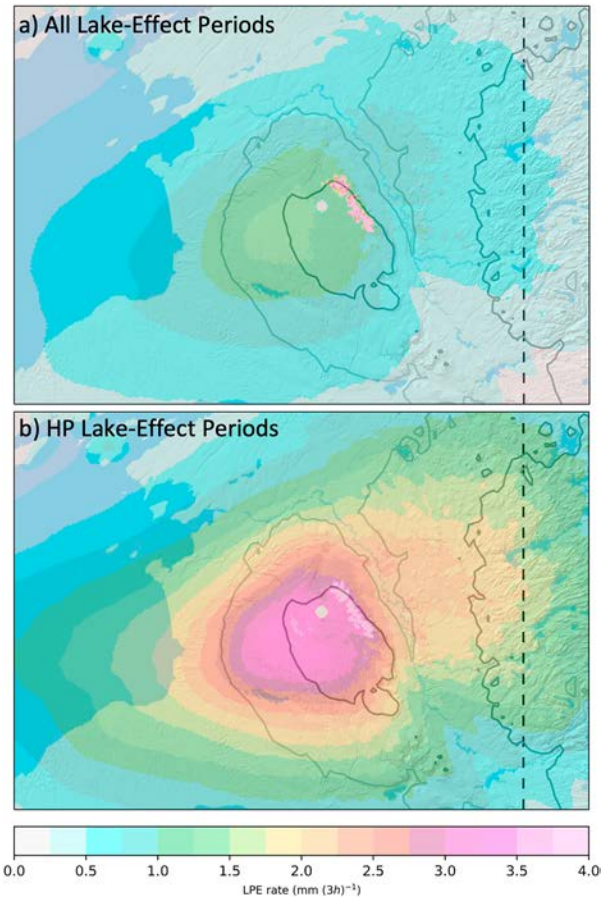


FIG. 4. Mean 3-h LPE rate [mm (3 h)$^{-1}$] during (a) all lake-effect periods ($n$ = 2184) and (b) HP lake-effect periods ($n$ = 434). The 250-m terrain contour (light solid line), 500-m terrain contour (dark solid line), and OLDF meridian (dashed line) are annotated.

LPE rate extends from the southeast shore of Lake Ontario to Tug Hill east of which it shifts poleward and extends eastward across the northern Black River valley and the western Adirondacks. Beam blockage to the southeast of KTYX may enhance this shift by reducing reflectivities and REP along southeast-oriented radials. Although complicated by the clutter effects of the wind farms, the mean LPE rate decreases over the eastern escarpment of Tug Hill, indicative of lee shadowing. Relatively high values of mean LPE rate extend over the northwestern Adirondack foothills before decreasing farther inland over the central Adirondacks. This decrease is consistent with mean annual snowfall climatologies (e.g., National Weather Service 2022; Steenburgh 2023, his Fig. 3.10), but may partly reflect overshooting or partial beam filling. Per figures from Brown et al. (2007), which assume standard refraction, the centroid of the lowest-level (0.5°) scan is at ~1.5 km MSL and ~1.0 km AGL 75 km from the KTYX radar, which roughly corresponds to the eastern edge of Fig. 4.

Histograms of maximum radar-estimated 3-h precipitation at the REDF and OLDF meridians illustrate changes in the characteristics of lake-effect precipitation from Tug Hill to

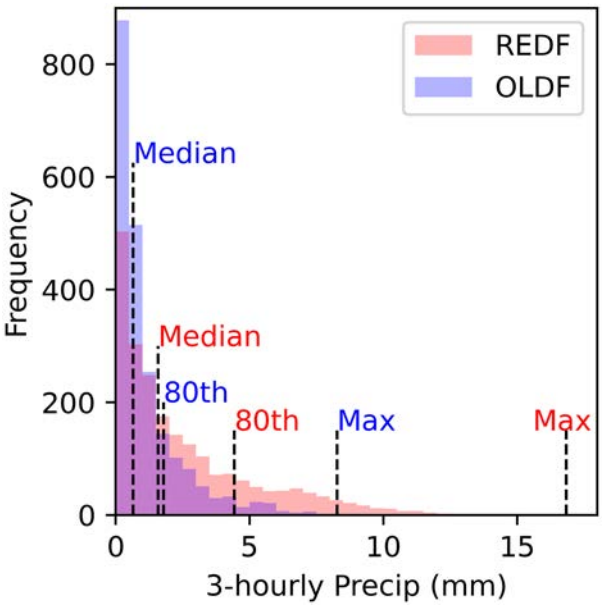


FIG. 5. Histogram of maximum 3-h precipitation along the REDF (red) and OLDF (blue) meridians. Median, 80th-percentile, and maximum values are annotated.

the western Adirondacks (Fig. 5). Consistent with a decline in the mean 3-h LPE rate inland from Tug Hill, the distribution of maximum 3-h precipitation over the western Adirondacks is shifted toward lower values. For example, the median and 80th-percentile maximum 3-h precipitation over the western Adirondacks are 0.7 and 1.8 mm, respectively, as compared with 1.6 and 4.4 over Tug Hill. The frequency of periods with a maximum 3-h accumulation at or above 1.8 mm, which corresponds to 2.5 cm of snow at climatological snow-to-liquid ratios (Baxter et al. 2005), declines by a factor of 2.3 from Tug Hill to the western Adirondacks.

The spatial distribution of mean LPE rate during HP periods over the western Adirondacks exhibits some similarities to all lake-effect periods such as a maximum over Tug Hill, a decrease over the eastern escarpment of Tug Hill, and an extension of high mean LPE rates over the western Adirondacks (cf. Figs. 4a,b). The mean LPE rate during HP periods, however, is much higher nearly everywhere, and especially over the western Adirondacks, indicating that western Adirondack HP periods are regionally stronger lake-effect storms and not enhanced locally. Additionally, the axis of maximum precipitation is more zonally oriented and closer to the mid-lake axis rather than the south shore of Lake Ontario. Such an orientation and alignment are favored by boundary layer flow from 250° to 270°, whereas a maximum along the south shore is favored by flow from 270° to 300° (Veals and Steenburgh 2015, see their Fig. 16).

### *b. Environmental conditions during HP periods over the western Adirondacks*

Next, we compared the environmental conditions during HP and non-HP periods in the western Adirondacks. HP periods

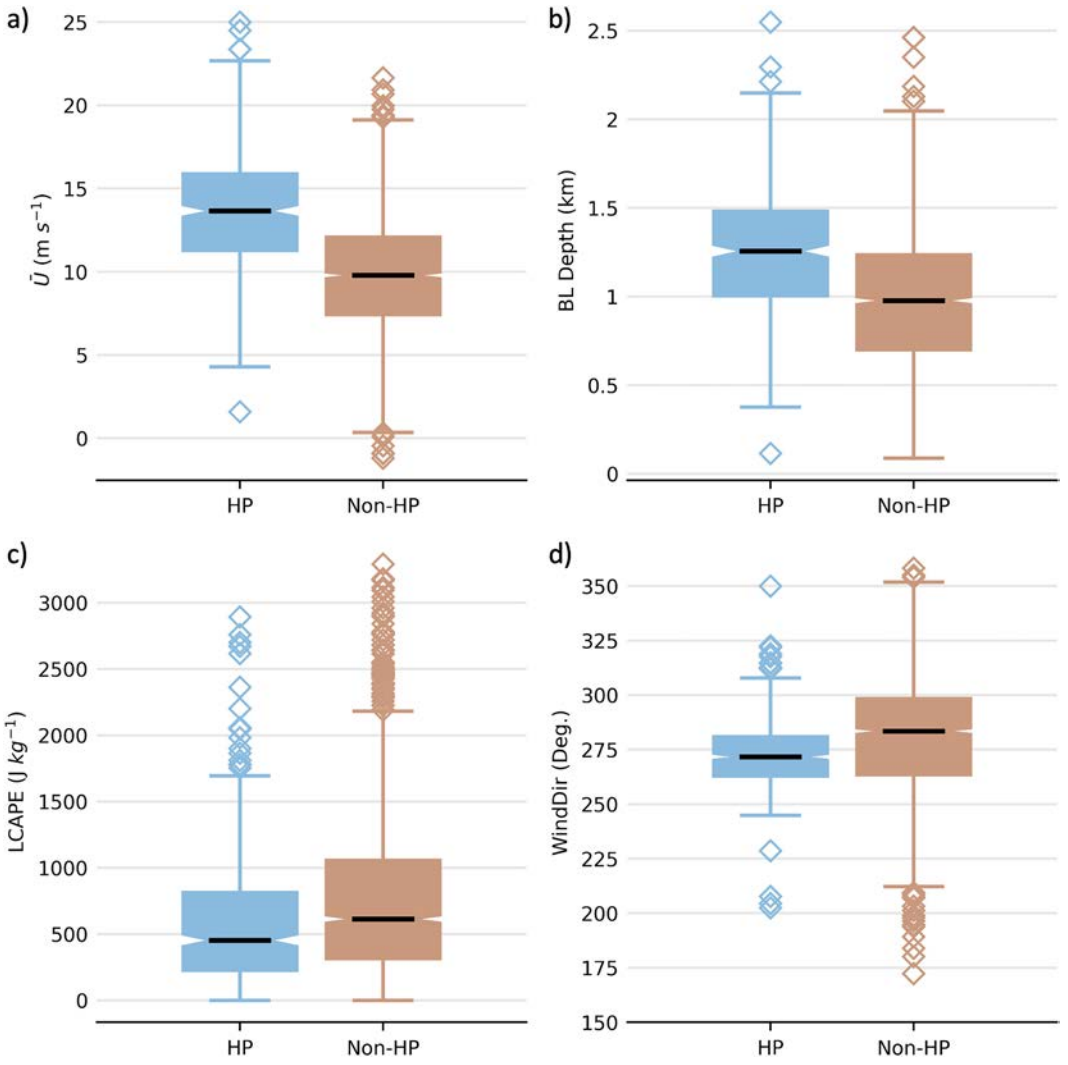


FIG. 6. Box-and-whisker plots depicting the distributions of (a) $\overline{U}$, (b) boundary layer depth, (c) LCAPE, and (d) boundary layer wind direction during HP (blue) and non-HP periods (brown). Whiskers and outliers are based on 1.5 times the interquartile range above the first and third quartile.

are generally characterized by higher $\overline{U}$ and deeper boundary layers than non-HP periods (Figs. 6a,b; in this and other box-and-whisker plots, boxes with notches that do not overlap indicate that the medians differ at a 95% confidence level). The former is broadly consistent with Veals et al. (2018) who found that strong incident boundary layer flow favors higher precipitation rates and greater inland and orographic precipitation enhancement over Tug Hill. In contrast, although higher LCAPE leads to greater precipitation enhancement over Tug Hill (Veals et al. 2018), there is a tendency for HP periods over the western Adirondacks to feature lower LCAPE (Fig. 6c). A comparable analysis using the daily lake-surface temperature from the Great Lakes Surface Environmental Analysis (GLSEA), however, showed a no significant difference between the medians of HP and non-HP events (not shown), so this relationship may be weak. Last, HP periods feature a narrower range of boundary layer wind directions than non-HP periods, with the interquartile range between 263° and 281° (Fig. 6d). Overall, these results, along with the more zonally elongated distribution of mean precipitation rate during HP periods than during non-HP periods (cf. Figs. 4a,b), highlight the importance of strong zonal flow for HP periods over the western Adirondacks.

To further highlight the roles of $\overline{U}$, boundary layer depth, and LCAPE, we divided the distribution for each variable

TABLE 1. Lower (low), middle (medium), and upper (high) quintiles for $\overline{U}$, boundary layer depth, and LCAPE during all lake-effect periods.

| | Low | Medium | High |
|---|---|---|---|
| $\overline{U}$ (m s$^{-1}$) | ≤7.25 | 9.51–11.42 | ≥13.78 |
| Boundary layer depth (m) | ≤679.4 | 923.0–1135.1 | ≥1378.4 |
| LCAPE (J kg$^{-1}$) | ≤226.3 | 457.5–730.5 | ≥1144.1 |

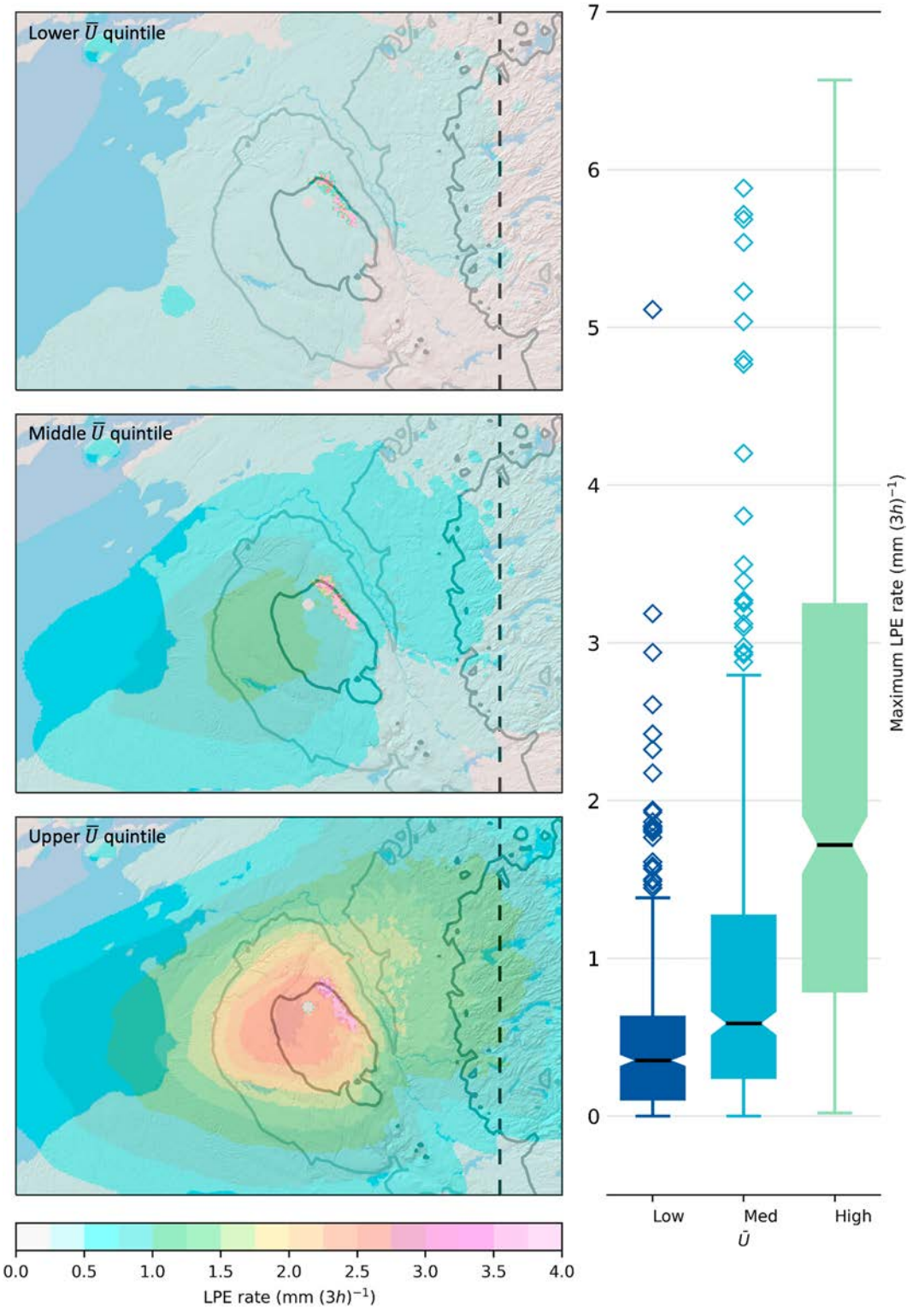


FIG. 7. Plan-view mean LPE rate [mm $(3\ \text{h})^{-1}$] and box-and-whisker plot of maximum LPE rate along the OLDF meridian during lower, middle, and upper $\overline{U}$ quintile periods. The 250-m terrain contour (light solid line), 500-m terrain contour (dark solid line), and OLDF meridian (dashed line) are annotated in the plan-view plots. Whiskers and outliers are based on 1.5 times the interquartile range above the first and third quartile.

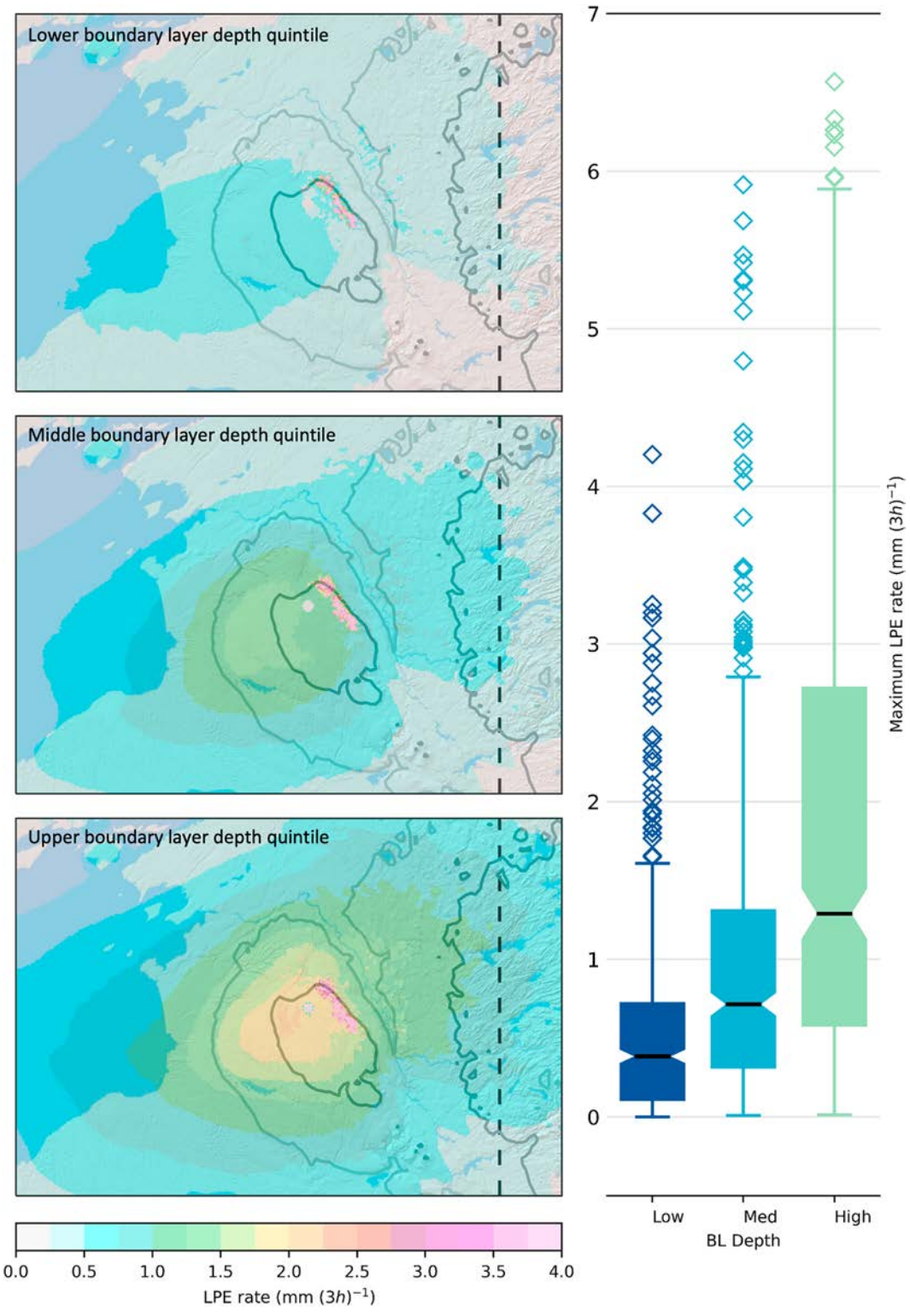


FIG. 8. As in Fig. 7, but for boundary layer depth.

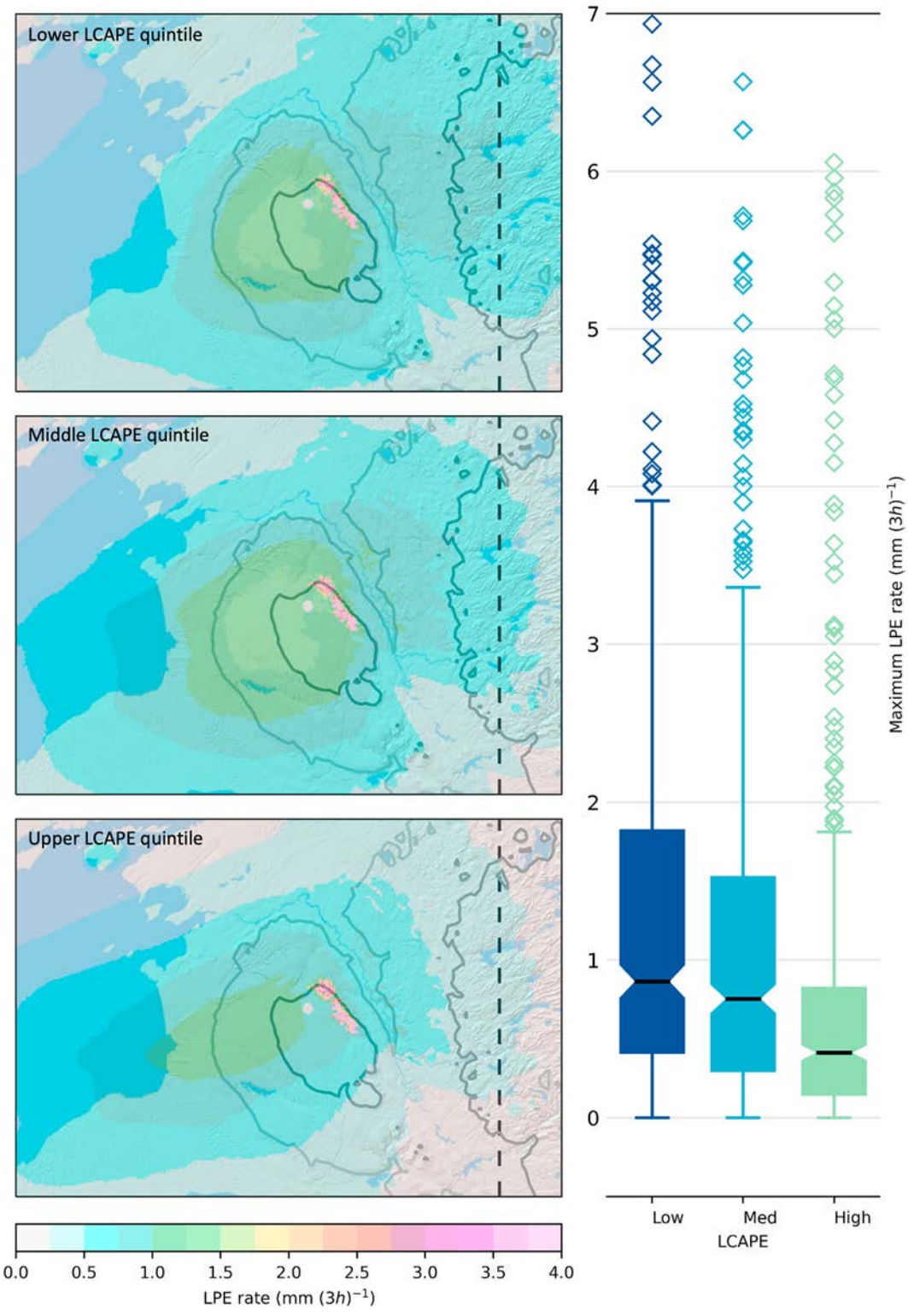


FIG. 9. As in Fig. 7, but for LCAPE.

during all lake-effect periods into quintiles and examined the precipitation distributions in the lower (low), middle (medium), and upper (high) quintiles, as defined in Table 1. Low $\overline{U}$ periods are associated with the lowest mean precipitation rates throughout the region, including the western Adirondacks (Fig. 7). In contrast, high $\overline{U}$ periods have the highest precipitation rates, including over the Black River valley and western Adirondacks. With increasing flow, the precipitation maximum shifts inland from near the Lake Ontario shoreline to upper Tug Hill, consistent with Veals et al. (2018). Although the variable nature of lake-effect precipitation yields a wide range of maximum LPE rate at the OLDF meridian for low, medium, and high $\overline{U}$, including some periods with no precipitation, there is a clear upward shift in the 25th, 50th, and 75th percentiles of maximum LPE rate with increasing $\overline{U}$ (see box-and-whiskers plot in Fig. 7). This indicates a greater likelihood of higher precipitation rate in the western Adirondacks for higher $\overline{U}$. For all categories, the poleward shift of the axis of maximum precipitation from Tug Hill to the western Adirondacks is present.

Throughout the region, including the western Adirondacks, precipitation increases with increasing boundary layer depth. Similarly, there is an upward shift in the 25th, 50th, and 75th percentiles of maximum LPE rate at the OLDF meridian (Fig. 8). For LCAPE, there is a tendency for the maximum LPE rate at the OLDF meridian to decline with increasing LCAPE (Fig. 9). This is broadly consistent with, Villani et al. (2017) who found a strong negative correlation between the inland extent of lake-effect precipitation features and the lake–850-hPa and lake–700-hPa temperature differences, which are closely related to LCAPE. This suggests that strong lake-induced instability may limit deep inland penetration of lake-effect precipitation.

To further illustrate the combination of $\overline{U}$ and boundary layer depth, we examined eight different combinations of low, medium, and high $\overline{U}$ and boundary layer depth and their relationship to the maximum 3-h precipitation rate at the OLDF meridian (Fig. 10). Low and medium $\overline{U}$ periods had medians of 0.7 mm or less, regardless of boundary layer depth. During high $\overline{U}$ periods, the median maximum 3-h precipitation rate increased with boundary layer depth and maximized at more than 2 mm for the combination of high $\overline{U}$ and high boundary layer depth. The largest events occurred for that combination as well. Low $\overline{U}$ and high boundary layer depth (10 periods) as well as high $\overline{U}$ and low boundary layer depth (4 periods) occur rarely, limiting the ability to draw conclusions from those categories.

We also examined precipitation distributions for mean boundary layer wind directions in 10° increments from 240° to 300° (e.g., 240°–250° = 240.00°–249.99°). The highest LPE rates occur for mean boundary layer winds from 260° to 270°, whereas the lowest LPE rates occur for mean boundary layer winds from 290° to 300° (Fig. 11). The region of maximum LPE rate shifts equatorward as the flow veers from 240°–250° to 290°–300°, consistent with synoptic expectations and the findings of Veals and Steenburgh (2015). The highest LPE rates in the western Adirondacks occur for mean boundary layer wind directions of 260°–270°. At the OLDF meridian,

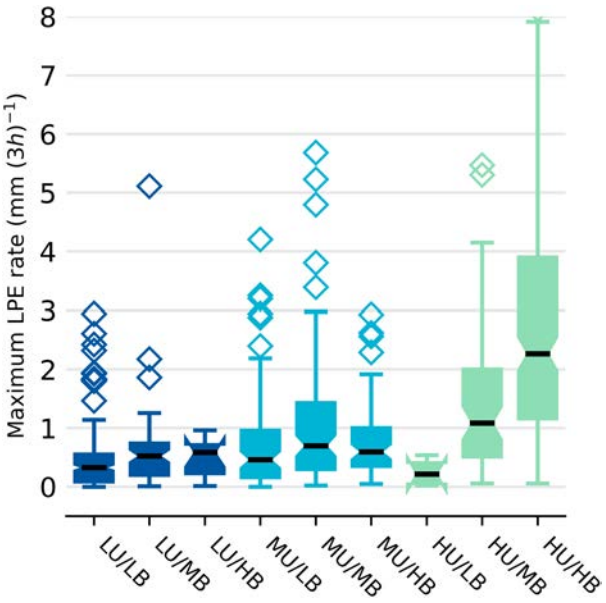


FIG. 10. Box-and-whisker plots depicting the distribution of maximum LPE rate [mm (3 h)$^{-1}$] along the OLDF meridian for different combinations of high (label H), moderate (label M), and low (label L) zonal wind speed (label U) and boundary layer depth (label B). Whiskers and outliers are based on 1.5 times the interquartile range above the first and third quartile.

the greatest median, 75th-percentile, and 90th-percentile maximum LPE rates are also greatest for 260°–270°, with the second highest values for 270°–280°, indicating the importance of zonal flow for western Adirondack lake-effect events (Fig. 12). For all boundary layer direction increments between 250° and 280°, there is a clear poleward shift of the axis of maximum precipitation and a narrowing of the precipitation region from Tug Hill to the Adirondacks (Fig. 11). Although this shift may partly reflect beam blockage to the southeast of the radar site, it is present even for mean boundary layer wind directions of 250°–260°. This suggests that the poleward shift and narrowing reflect a physical process, perhaps related to downslope effects in the lee of Tug Hill.

Morphology influences the intensity and spatial distribution of lake-effect precipitation (e.g., Laird et al. 2003; Campbell et al. 2016; Veals et al. 2018) and may have an additional influence on lake-effect precipitation over the western Adirondacks. As described in section 2a, this analysis is based on a subset of cases from Veals et al. (2018) during the 2012/13–2016/17 cool seasons in which the morphology of the lake-effect precipitation features was identified in 3-h intervals along a transect at 43.62°N (Figs. 1a,b). Banded periods have a narrow, strong precipitation distribution, while nonbanded periods are broader and less intense (Fig. 13). Both types of periods illustrate a sharp decrease in LPE rate into the Black River valley, though banded periods indicate higher western Adirondack precipitation over nonbanded periods.

Detailed airborne and in situ observations from OWLeS can help better illustrate the inland transition and orographic modification of LE snow over the sparsely populated and

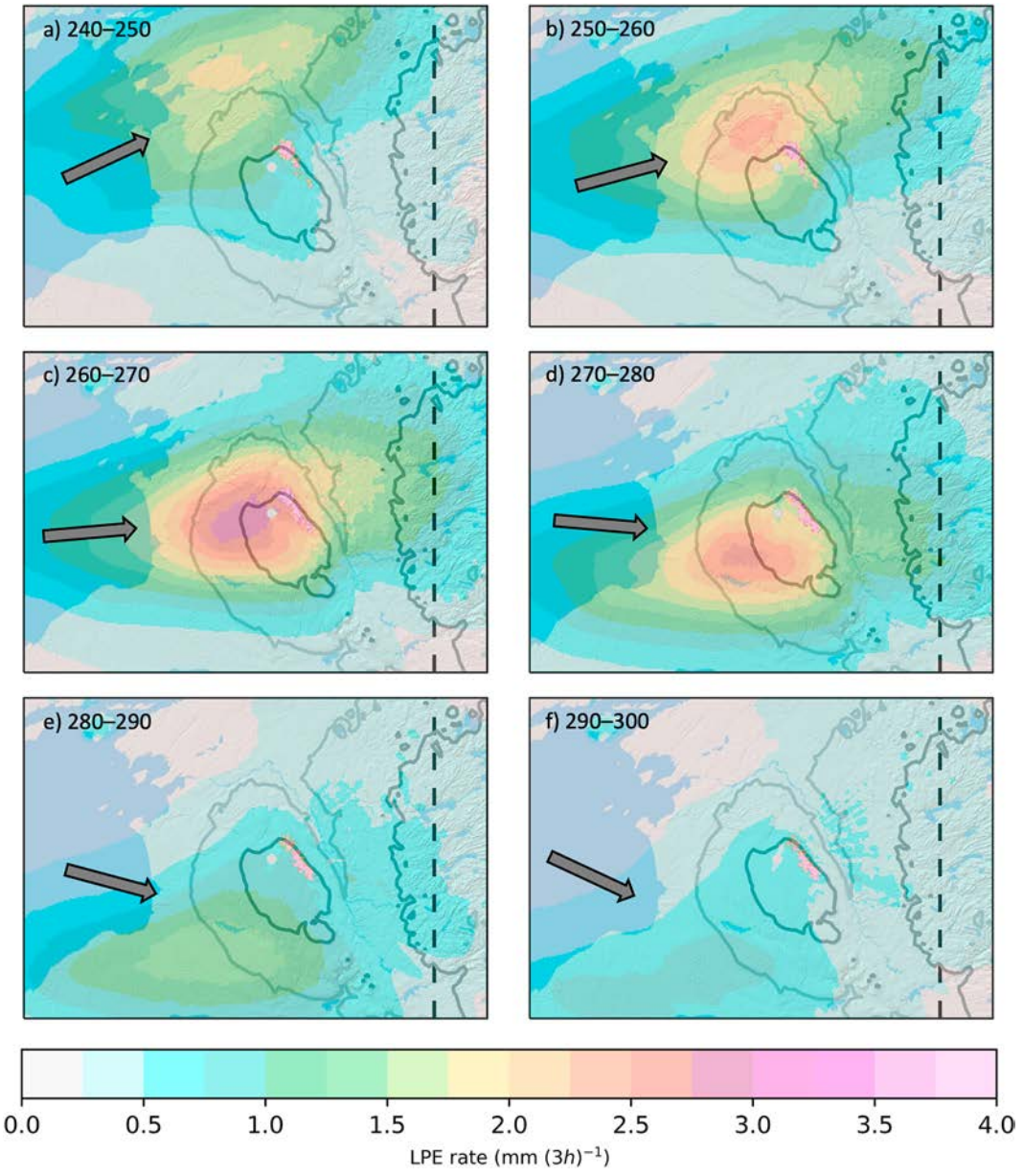


FIG. 11. Plan view of mean LPE rate for (a) 240°–250°, (b) 250°–260°, (c) 260°–270°, (d) 270°–280°, (e) 280°–290°, and (f) 290°–300° boundary layer wind directions. The 250-m terrain contour (light solid line), 500-m terrain contour (dark solid line), and OLDF meridian (dashed line) are annotated.

observationally limited western Adirondacks. As part of OWLeS, two UWKA flights were conducted between Lake Ontario and the western Adirondacks, one in IOP10 on 12 January 2014, and one in IOP14 on 19 January 2014. The latter featured strong turbulence along the flight leg, especially in the lowest km above the terrain, enabling the ~2-km deep cloud and snow layer to be maintained eastward into the central Adirondacks (Welsh et al. 2014). However, it was a weak event, and there were no KTYX radar data available to provide spatial and temporal context. Therefore, we focus here on IOP10 during which KTYX radar data is available.

### c. *Airborne radar analysis OWLeS IOP10*

IOP10 was a lake-orographic event with weak, quasi-stationary radar echoes forming downstream of Lake Ontario over Tug Hill and the western Adirondacks. During IOP10, the UWKA flew a single along-wind flight leg from the central Adirondacks westward over the Black River valley, Tug Hill, and the eastern end of Lake Ontario from 1359 to 1434 UTC. A sounding collected from North Redfield one hour prior to the start of this leg at 1259 UTC revealed an ~1.3-km deep surface-based mixed layer with predominantly westerly flow

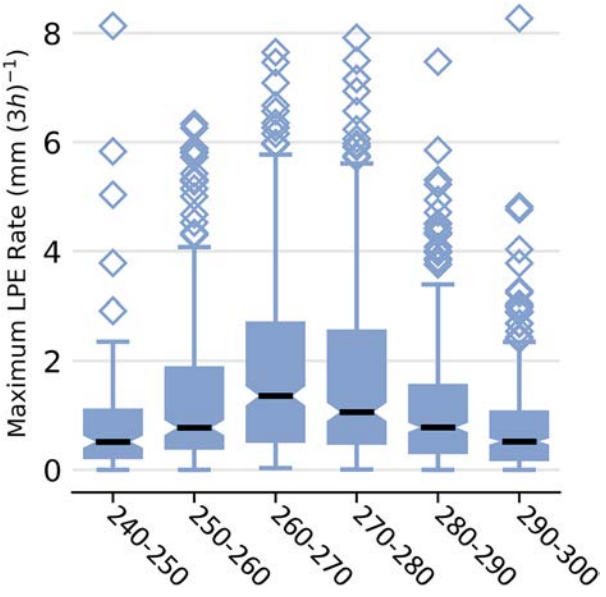


FIG. 12. Box-and-whisker plots depicting the distribution of maximum LPE rate [mm (3 h)$^{-1}$] along the OLDF meridian with wind direction. Whiskers and outliers are based on 1.5 times the interquartile range above the first and third quartile.

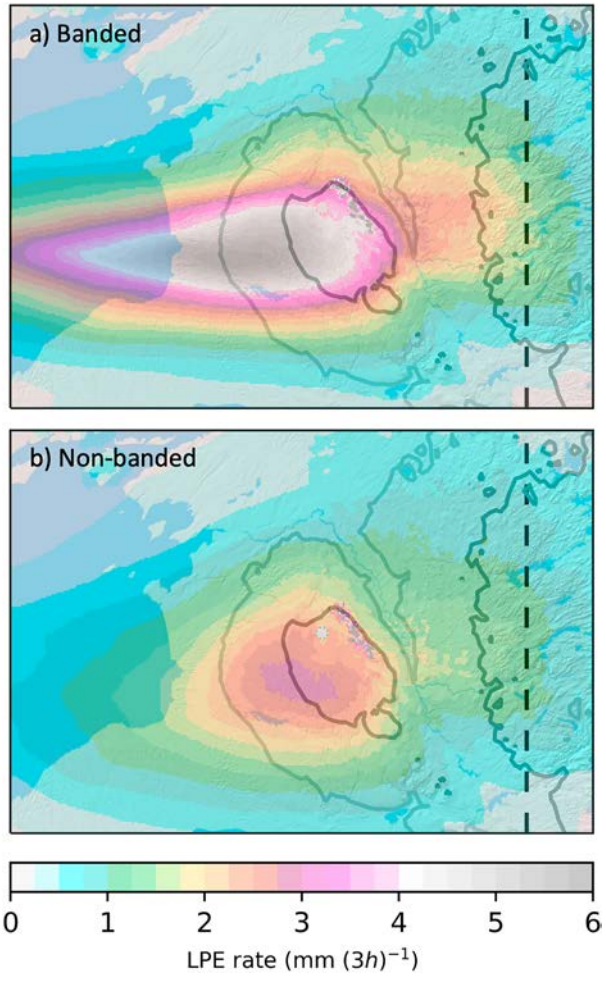


FIG. 13. Mean LPE rate [mm (3 h)$^{-1}$] for (a) banded and (b) nonbanded lake-effect periods. Scale is extended into grayscale up to 6 mm (3 h)$^{-1}$. The 250-m terrain contour (light solid line), 500-m terrain contour (dark solid line), and OLDF meridian (dashed line) are annotated.

from Lake Ontario (Fig. 14). This mixed layer was capped by an isothermal stable layer in which the flow veered to the northwest. Above this isothermal layer a second well-mixed layer extended from 780 to 720 hPa. The origin of this elevated mixed layer is unclear but given the more northwesterly flow it may represent lake-modified air from Lake Huron. Except within a few hundred meters of the surface, the flow within these layers was strong and generally 18–20 m s$^{-1}$. For this sounding, $\overline{U}$ = 18.5 m s$^{-1}$, the boundary layer depth was 1.3 km, and the LCAPE was ~190 J kg$^{-1}$ based on a $T_{\text{lake}}$ of 2.1°C obtained from GLSEA analysis. A comparison of this case with the 8-yr climatology (section 3a) places this case in the upper quintile for $\overline{U}$, near the upper quintile for boundary layer depth, and in the lower quintile for LCAPE (Table 1).

KTYX radar at the start of the flight leg at 1401 UTC showed a broad region of precipitation over and south of Tug Hill with evidence of weak banding extending inland from the southeast shore of Lake Ontario (Fig. 15a). Reflectivities decreased over the Black River valley (the radial stripes over this valley were from multipath scattering from the wind farms over Tug Hill) and then increased over the western Adirondacks. This pattern is similar to the lake-orographic pattern described by Veals and Steenburgh (2015). It persisted during the UWKA flight leg that crosses the apparent orographic features over the western Adirondacks and Tug Hill but remained near or just north of the weak band extending inland from southeast Lake Ontario (Fig. 15b).

The WCR observations are consistent with the inferred orographic influences on precipitation described above with stratiform precipitation developing over the windward slope of Tug Hill and falling out over the upper Tug Hill ($10 < x < 65$ km in Fig. 16a). This precipitation is orographically enhanced since there is net rising air motion over the western slope of Tug Hill ($8 < x < \sim 40$ km in Fig. 16b). A shallow turbulent layer characterized by small-scale variability in air vertical velocity (Fig. 16b) and decelerated flow relative to that aloft (Fig. 16c) develops near the lake shore, deepens over the western slope of Tug Hill, and extends inland across the Black River valley and Adirondacks, reaching depths of a few hundred meters. It is unclear if this turbulence contributed to cloud and precipitation processes. Farther inland, precipitation spillover and downslope flow occur over Tug Hill's steeper eastern slope ($65 < x < 75$ km). WCR radar echoes weaken eastward across the Black River valley and into the far western Adirondacks ($75 < x < 95$ km), consistent with the KTYX map view (Fig. 15). Broad ascent occurs over the eastern Black River valley, possibly associated with a resonant lee wave between Tug Hill and the Adirondacks (e.g., Grubišić and Stiperski 2009; Geerts et al. 2023). This ascent, which tilts upstream with height, deepens the cloud layer and increases echo-top heights aloft ($60 < x < 75$). Precipitation invigorates farther

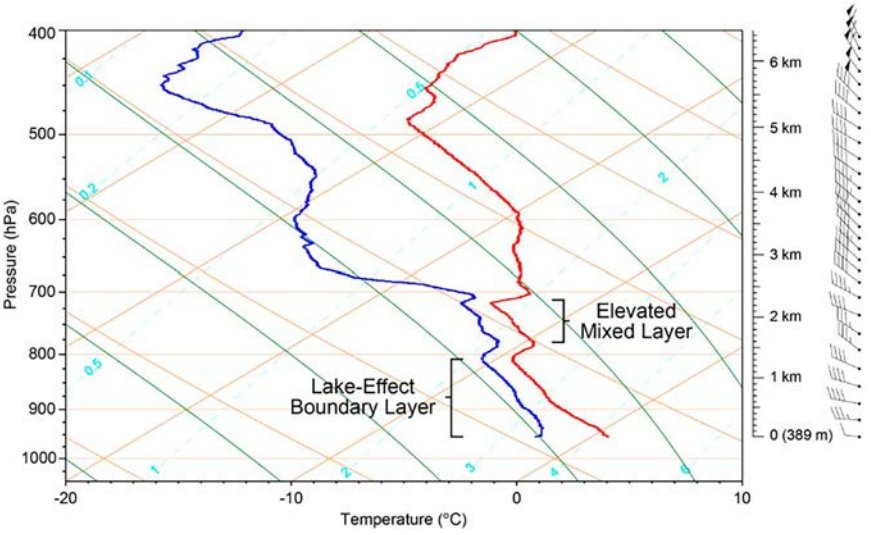


FIG. 14. North Redfield skew $T$–log$p$ diagram [temperature (red); dewpoint (blue)] at 1259 UTC 12 Jan 2014. Full and half barbs indicate 5 and 2.5 m s$^{-1}$, respectively.

east over the Adirondacks ($95 < x < 145$ km) where WCR reflectivities exceed those over Tug Hill, in contrast to the KTYX reflectivity (Fig. 15), which may be affected by partial overshooting of the shallow (<2.7 km MSL) echoes. Hydrometeor streamlines that appear to originate near the top of the deepened cloud layer associated with the resonant lee-wave updraft between Tug Hill and the Adirondacks approach the surface in the region of increasing low-level reflectivity ($90 < x < 105$; Fig. 16a). This region is still windward of the highest peaks of the central Adirondacks and contained pockets of supercooled liquid water (observed at flight level; not shown) that may enhance snow growth, as observed elsewhere (Geerts et al. 2023).

Throughout the flight leg, small-scale cloud-top-generating cells were present near and above flight level (Fig. 16a). These features are common over stratiform cloud tops (e.g., Rosenow et al. 2014; Keeler et al. 2016a,b) and are driven mainly by radiative cooling, which destabilizes the cloud-top region (Keeler et al. 2016b). This may explain most of the convective motions seen in the vertical velocity data above ~2 km MSL (Fig. 16b).

The analysis described above illustrates that the relatively modest Tug Hill and western Adirondacks strongly influence precipitation during this lake-orographic event. Wind speeds during this event were very high (18–20 m s$^{-1}$) and westerly, and the boundary layer was deep. Both factors favor deep inland penetration of lake-effect systems, as shown in section 2b. The case, however, was predominantly nonbanded, which favors lower precipitation rates, but also greater orographic enhancement (Veals et al. 2018). Terrain-induced ascent on the windward side of Tug Hill appeared to enhance precipitation over upper Tug Hill, with spillover across the eastern escarpment. Subsidence into the Black River valley appeared to weaken precipitation. Boundary layer deepening and precipitation invigoration occurred farther eastward, driven by the resonant updraft in the lee of Tug Hill, and the gradual mean terrain-induced ascent over the western Adirondacks. OWLeS did not examine a LLAP-band event inland over the Black River valley and western Adirondacks, so the existence and potential role of such terrain-induced features on that lake-effect morphology awaits future modeling or field-program activities.

## 4. Conclusions

The characteristics of inland penetrating lake-effect storms east of Lake Ontario are modulated by the ambient flow, lake-effect mode, and the modest topography of Tug Hill, the Black River valley, and western Adirondacks in New York. Radar statistics from the Montague/Fort Drum (KTYX) WSR-88D illustrate that mean precipitation during lake-effect periods maximizes over Tug Hill and decreases abruptly where the Tug Hill escarpment drops into the Black River valley. The axis of maximum precipitation shifts poleward from Tug Hill to the western Adirondacks where precipitation decreases eastward (and downwind) into the central Adirondacks. Strong zonal boundary layer flow, greater boundary layer depths, and the organization of lake-effect precipitation into a LLAP-band generate the highest precipitation rates over the western Adirondacks. Both banded (i.e., LLAP band) and nonbanded lake-effect periods feature a decrease in mean LPE rate from Tug Hill into the Black River valley, but banded periods generally feature higher LPE rates in the western Adirondacks. Maximum LPE rates in the western Adirondacks did appear to decline with increasing LCAPE, consistent with prior studies indicating an inverse correlation between lake–850-hPa and lake–700-hPa temperature differences and the inland penetration of lake-effect systems (e.g., Villani et al. 2017).

These findings are consistent with prior literature. Zonal flow maximizes the fetch over Lake Ontario and strong boundary layer winds promote increased latent and sensible heat fluxes (e.g., DeCosmo et al. 1996; Veron et al. 2008) and

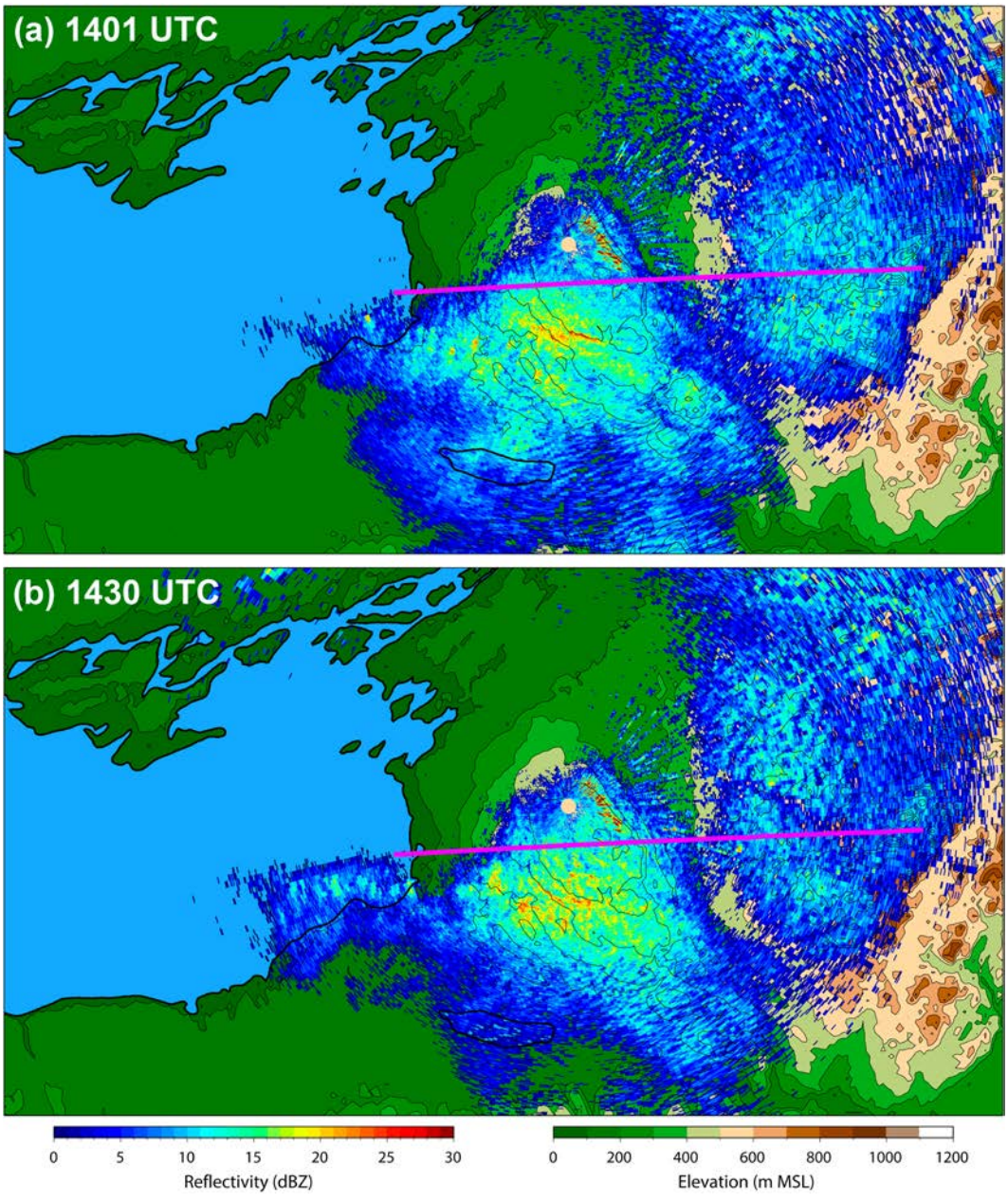


FIG. 15. KTYX 0.5° base reflectivity at (a) 1401 and (b) 1430 UTC 12 Jan 2014 overlaid on topography (the scales are given at the bottom). Magenta lines indicate the UWKA along-wind flight leg.

have been shown to produce deep inland penetration of lake-effect storms in multiple regions (Villani et al. 2017; Eipper et al. 2018, 2019; Veals et al. 2018, 2019, 2020). The stronger flow and deeper boundary layer (and hence lake-effect system depth) also favor downstream transport of hydrometeors, including spillover across Tug Hill and into the Black River valley, as observed across other topographic features (e.g., Sinclair et al. 1997). Additionally, consistent with our climatology, lake-effect systems with shallower boundary layers are often weaker (Hjelmfelt 1990) and may dissipate before reaching the western Adirondacks (e.g., Hjelmfelt 1990; Reinking et al. 1993). Overall, these and prior results indicate that the strength of the incident flow and the depth of the lake-effect system are critical factors for the penetration of lake-effect systems to inland topographic features.

Analysis of Wyoming Cloud Radar (WCR) data collected by the University of Wyoming King Air (UWKA) during OWLeS IOP10 revealed several key impacts of Tug Hill, the Black River valley, and western Adirondacks on a nonbanded, lake-orographic event with strong winds and a deep boundary layer. Specifically, upslope flow enhanced precipitation over Tug Hill, which spilled across the Tug Hill escarpment. A resonant

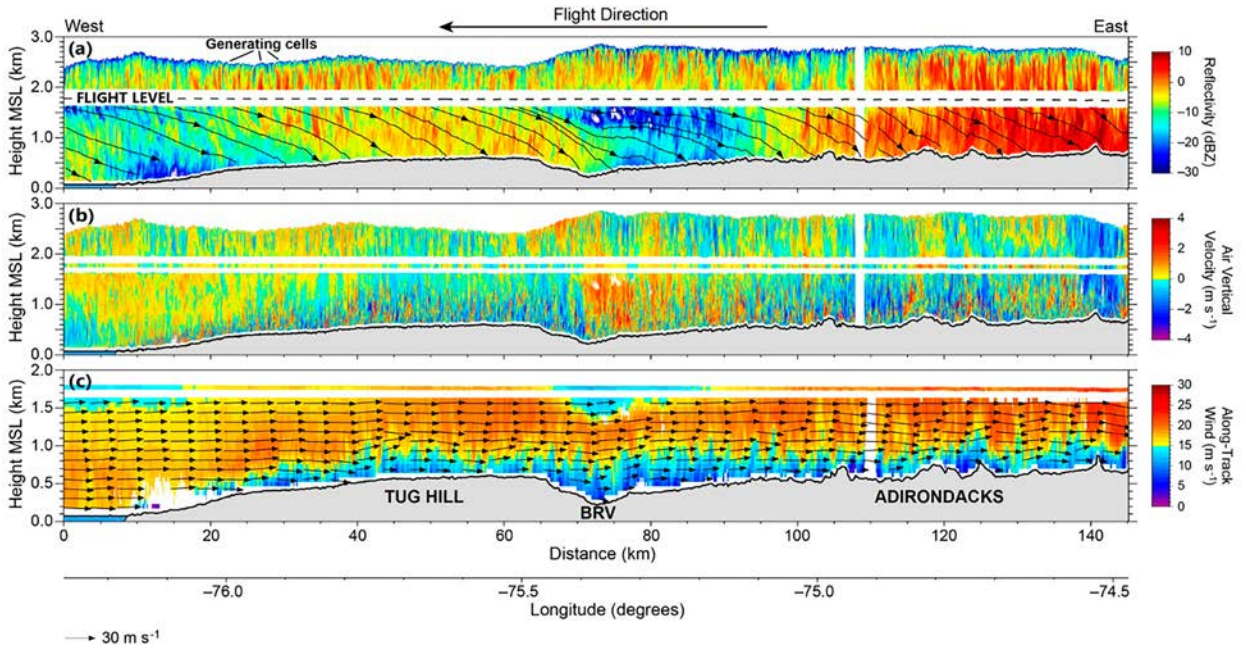


FIG. 16. WCR observations from the along-wind flight leg (1359–1434 UTC 12 Jan 2014): (a) reflectivity above and below flight level and hydrometeor streamlines ($u$, $w_H$) below flight level, (b) air vertical velocity $w$ above and below flight level, and (c) dual-Doppler along-track horizontal wind speed $u$ and 2D wind vectors ($u$, $w$) below flight level (note the change in the $y$ axis). The black dashed line in (a) shows the UWKA flight level, which sits within an ~200-m-deep radar blind zone. The gap of missing data at $x$ = ~110 km is due to a WCR beam scrambling issue during flight. The slight misalignment of this gap in (c) is an artifact of the dual-Doppler data being projected onto a straight 2D grid (the actual flight leg was not perfectly straight). Labeled at the surface are Tug Hill, the BRV, and the Adirondacks.

lee wave appeared to be present over the Black River valley, which led to a deepening of the lake-effect cloud layer. Echoes were weaker over the western Black River valley and initial slopes of the western Adirondacks before invigoration farther downstream. This invigoration occurred in a region where hydrometeor streamlines originating near the top of the deeper cloud layer finally approach the ground in a region still windward of the highest peaks of the central Adirondacks. Boundary layer turbulence developed and deepened immediately downstream of the Lake Ontario coast and extended inland across Tug Hill, the Black River valley, and the Adirondacks, although what role this played in the precipitation evolution is unclear. Small-scale cloud-top-generating cells were observed near and above flight level and contributed to precipitation processes during the inland penetration of the storm system but were likely related to cloud-top radiative cooling rather than an orographic effect.

Although these findings help to illustrate the factors affecting the inland penetration and orographic modulation of lake-effect precipitation east of Lake Ontario, further work is needed to better elucidate the case-to-case variations in terrain-induced flows and their influence on spillover downstream of Tug Hill and the evolution of lake-effect systems over the western Adirondacks. In particular, WCR profiles similar to those presented in Fig. 16 could be used to illustrate variations in orographic circulations and precipitation features across a wider range of ambient flows and lake-effect modes, especially LLAP bands that tend to produce the heaviest precipitation over the western Adirondacks. Such bands were not examined over the Adirondacks during OWLeS. Such data could also be used to validate next-generation convection permitting ensemble systems [e.g., the Rapid Refresh Forecast System (RRFS)] and ultimately improve forecasts for rural communities, mountain transport, and winter recreation in the lake-effect snowbelt east of Lake Ontario.

*Acknowledgments.* This material is based on work supported by the National Science Foundation under Grant AGS-1929602 and AGS-1258856, NOAA/National Weather Service CSTAR Program Grant NA20NWS4680046A, and NASA Grant 80NSSC20M0113. Any opinions, findings, and conclusions or recommendations expressed in this material are those of the authors and do not necessarily reflect the views of the National Science Foundation, NOAA/National Weather Service, or NASA. We thank NCEI, the New York State Mesonet, ECMWF, NCAR Earth Observing Laboratory, and GLERL for the provision of datasets. Original funding for the NYS Mesonet was provided by Federal Emergency Management Agency grant FEMA-4085-DR-NY, with the continued support of the NYS Division of Homeland Security and Emergency Services; the state of New York; the Research Foundation for the State University of New York (SUNY); the University at Albany; the Atmospheric Sciences Research Center (ASRC) at the University at Albany; and the Department

of Atmospheric and Environmental Sciences (DAES) at the University at Albany. The NCAR Earth Observing Laboratory is sponsored by the National Science Foundation. We also acknowledge the University of Utah Center for High Performance Computing for computer support and everyone who participated in the OWLeS field campaign. John Horel, Courtenay Strong, and David Kingsmill provided valuable input and suggestions for the research.

*Data availability statement.* KTYX WSR-88D data are available from the National Centers from Environmental Information (https://www.ncei.noaa.gov/products/radar) or AWS (https://registry.opendata.aws/noaa-nexrad/). New York State Mesonet data are available online (https://www2.nysmesonet.org/weather/requestdata). ERA5 reanalysis data are available from the Copernicus Climate Change Service Climate Data Store (https://cds.climate.copernicus.eu/cdsapp#!/home). The Great Lakes Surface Environmental Analysis (GLSEA) lake-surface temperature data are available from the NOAA Great Lakes Environmental Research Laboratory Daily GLSEA NetCDF Depot: SST (https://www.glerl.noaa.gov/res/glcfs/). UWKA WCR and other OWLeS datasets are available from the NCAR Earth Observing Laboratory OWLeS data access site (https://www.eol.ucar.edu/field_projects/owles).

## REFERENCES

Baxter, M. A., C. E. Graves, and J. T. Moore, 2005: A climatology of snow-to-liquid ratio for the contiguous United States. *Wea. Forecasting*, **20**, 729–744, https://doi.org/10.1175/WAF856.1.

Bergmaier, P. T., B. Geerts, L. S. Campbell, and W. J. Steenburgh, 2017: The OWLeS IOP2b lake-effect snowstorm: Dynamics of the secondary circulation. *Mon. Wea. Rev.*, **145**, 2437–2459, https://doi.org/10.1175/MWR-D-16-0462.1.

Black River Watershed Management Plan, 2010: Part I: Watershed characterization, recommendations, and implementation. Final Rep., 220 pp., https://tughill.org/wp-content/uploads/2011/10/7BRWFinalDocumentPartI-May2010.pdf.

Brady, R. H., and J. S. Waldstreicher, 2001: Observations of mountain wave-induced precipitation shadows over northeast Pennsylvania. *Wea. Forecasting*, **16**, 281–300, https://doi.org/10.1175/1520-0434(2001)016<0281:OOMWIP>2.0.CO;2.

Braham, R. R., 1983: The Midwest snow storm of 8–11 December 1977. *Mon. Wea. Rev.*, **111**, 253–272, https://doi.org/10.1175/1520-0493(1983)111<0253:TMSSOD>2.0.CO;2.

Brotzge, J. A., and Coauthors, 2020: A technical overview of the New York State Mesonet standard network. *J. Atmos. Oceanic Technol.*, **37**, 1827–1845, https://doi.org/10.1175/JTECH-D-19-0220.1.

Brown, R. A., T. A. Niziol, N. R. Donaldson, P. I. Joe, and V. T. Wood, 2007: Improved detection using negative elevation angles for mountaintop WSR-88Ds. Part III: Simulations of shallow convective activity over and around Lake Ontario. *Wea. Forecasting*, **22**, 839–852, https://doi.org/10.1175/WAF1019.1.

Byrd, G. P., R. A. Anstett, J. E. Heim, and D. M. Usinski, 1991: Mobile sounding observations of lake-effect snow bands in western and central New York. *Mon. Wea. Rev.*, **119**, 2323–2332, https://doi.org/10.1175/1520-0493(1991)119<2323:MSOOLE>2.0.CO;2.

Campbell, L. S., and W. J. Steenburgh, 2017: The OWLeS IOP2b lake-effect snowstorm: Mechanisms contributing to the Tug Hill precipitation maximum. *Mon. Wea. Rev.*, **145**, 2461–2478, https://doi.org/10.1175/MWR-D-16-0461.1.

——, ——, P. G. Veals, T. W. Letcher, and J. R. Minder, 2016: Lake-effect mode and precipitation enhancement over the Tug Hill Plateau during OWLeS IOP2b. *Mon. Wea. Rev.*, **144**, 1729–1748, https://doi.org/10.1175/MWR-D-15-0412.1.

Chater, A. M., and A. P. Sturman, 1998: Atmospheric conditions influencing the spillover of rainfall to lee of the Southern Alps, New Zealand. *Int. J. Climatol.*, **18**, 77–92, https://doi.org/10.1002/(SICI)1097-0088(199801)18:1<77::AID-JOC218>3.0.CO;2-M.

DeCosmo, J., K. B. Katsaros, S. D. Smith, R. J. Anderson, W. A. Oost, K. Bumke, and H. Chadwick, 1996: Air-sea exchange of water vapor and sensible heat: The Humidity Exchange Over the Sea (HEXOS) results. *J. Geophys. Res.*, **101**, 12 001–12 016, https://doi.org/10.1029/95JC03796.

Eipper, D. T., G. S. Young, S. J. Greybush, S. Saslo, T. D. Sikora, and R. D. Clark, 2018: Predicting the inland penetration of long-lake-axis-parallel snowbands. *Wea. Forecasting*, **33**, 1435–1451, https://doi.org/10.1175/WAF-D-18-0033.1.

——, S. J. Greybush, G. S. Young, S. Saslo, T. D. Sikora, and R. D. Clark, 2019: Lake-effect snowbands in baroclinic environments. *Wea. Forecasting*, **34**, 1657–1674, https://doi.org/10.1175/WAF-D-18-0191.1.

Frech, M., and J. Seltmann, 2017: The influence of wind turbines on dualpol radar moments and products. *38th Conf. on Radar Meteorology*, Chicago, IL, Amer. Meteor. Soc., 8 pp., https://ams.confex.com/ams/38RADAR/mediafile/Manuscript/Paper320487/ams_radar2017_frech_seltmann_WEA_4.pdf.

Fujisaki-Manome, A., D. M. Wright, G. E. Mann, E. J. Anderson, P. Chu, C. Jablonowski, and S. G. Benjamin, 2022: Forecasting lake-/sea-effect snowstorms, advancement, and challenges. *Wiley Interdiscip. Rev.: Water*, **9**, e1594, https://doi.org/10.1002/wat2.1594.

Geerts, B., Y. Yang, R. Rasmussen, S. Haimov, and B. Pokharel, 2015: Snow growth and transport patterns in orographic storms as estimated from airborne vertical-plane dual-Doppler radar data. *Mon. Wea. Rev.*, **143**, 644–665, https://doi.org/10.1175/MWR-D-14-00199.1.

——, C. Grasmick, R. M. Rauber, T. J. Zaremba, L. Xue, and K. Friedrich, 2023: Vertical motions forced by small-scale terrain and cloud microphysical response in extratropical precipitation systems. *J. Atmos. Sci.*, **80**, 649–669, https://doi.org/10.1175/JAS-D-22-0161.1.

Gowan, T. M., W. J. Steenburgh, and J. R. Minder, 2021: Downstream evolution and coastal-to-inland transition of landfalling lake-effect systems. *Mon. Wea. Rev.*, **149**, 1023–1040, https://doi.org/10.1175/MWR-D-20-0253.1.

——, ——, and ——, 2022: Orographic effects on landfalling lake-effect systems. *Mon. Wea. Rev.*, **150**, 2013–2031, https://doi.org/10.1175/MWR-D-21-0314.1.

Grubišić, V., and I. Stiperski, 2009: Lee-wave resonances over double bell-shaped obstacles. *J. Atmos. Sci.*, **66**, 1205–1228, https://doi.org/10.1175/2008JAS2885.1.

Helmus, J. J., and S. M. Collis, 2016: The Python ARM Radar Toolkit (Py-ART), a library for working with weather radar data in the Python programming language. *J. Open Res. Software*, **4**, e25, https://doi.org/10.5334/jors.119.

Hersbach, H., and Coauthors, 2020: The ERA5 global reanalysis. *Quart. J. Roy. Meteor. Soc.*, **146**, 1999–2049, https://doi.org/10.1002/qj.3803.

Hill, J. D., 1971: Snow squalls in the lee of Lake Erie and Ontario: A review of the literature. NOAA Tech. Memo. NWS ER-43, 20 pp., https://repository.library.noaa.gov/view/noaa/6330.

Hjelmfelt, M. R., 1990: Numerical study of the influence of environmental conditions on lake-effect snowstorms over Lake Michigan. *Mon. Wea. Rev.*, **118**, 138–150, https://doi.org/10.1175/1520-0493(1990)118<0138:NSOTIO>2.0.CO;2.

——, and R. R. Braham, 1983: Numerical simulation of the airflow over Lake Michigan for a major lake-effect snow event. *Mon. Wea. Rev.*, **111**, 205–219, https://doi.org/10.1175/1520-0493(1983)111<0205:NSOTAO>2.0.CO;2.

Hoyt, W. G., and W. B. Langbein, 1955: *Floods*. Princeton University Press, 469 pp.

Jones, E. A., C. E. Lang, and N. F. Laird, 2022: The contribution of lake-effect snow to annual snowfall totals in the vicinity of Lakes Erie, Michigan, and Ontario. *Front. Water*, **4**, 782910, https://doi.org/10.3389/frwa.2022.782910.

Keeler, J. M., B. F. Jewett, R. M. Rauber, G. M. McFarquhar, R. M. Rasmussen, L. Xue, C. Liu, and G. Thompson, 2016a: Dynamics of cloud-top generating cells in winter cyclones. Part I: Idealized simulations in the context of field observations. *J. Atmos. Sci.*, **73**, 1507–1527, https://doi.org/10.1175/JAS-D-15-0126.1.

——, ——, ——, ——, ——, ——, ——, and ——, 2016b: Dynamics of cloud-top generating cells in winter cyclones. Part II: Radiative and instability forcing. *J. Atmos. Sci.*, **73**, 1529–1553, https://doi.org/10.1175/JAS-D-15-0127.1.

Kelly, R. D., 1982: A single Doppler radar study of horizontal-roll convection in a lake-effect snow storm. *J. Atmos. Sci.*, **39**, 1521–1531, https://doi.org/10.1175/1520-0469(1982)039<1521:ASDRSO>2.0.CO;2.

——, 1984: Horizontal roll and boundary-layer interrelationships observed over Lake Michigan. *J. Atmos. Sci.*, **41**, 1816–1826, https://doi.org/10.1175/1520-0469(1984)041<1816:HRABLI>2.0.CO;2.

——, 1986: Mesoscale frequencies and seasonal snowfalls for different types of Lake Michigan snow storms. *J. Climate Appl. Meteor.*, **25**, 308–312, https://doi.org/10.1175/1520-0450(1986)025<0308:MFASSF>2.0.CO;2.

Kristovich, D. A. R., 1993: Mean circulations of boundary-layer rolls in lake-effect snowstorms. *Bound.-Layer Meteor.*, **63**, 293–315, https://doi.org/10.1007/BF00710463.

——, N. F. Laird, M. R. Hjelmfelt, R. G. Derickson, and K. A. Cooper, 1999: Transitions in boundary layer meso-γ convective structures: An observational case study. *Mon. Wea. Rev.*, **127**, 2895–2909, https://doi.org/10.1175/1520-0493(1999)127<2895:TIBLMC>2.0.CO;2.

——, and Coauthors, 2017: The Ontario Winter Lake-effect Systems field campaign: Scientific and educational adventures to further our knowledge and prediction of lake-effect storms. *Bull. Amer. Meteor. Soc.*, **98**, 315–332, https://doi.org/10.1175/BAMS-D-15-00034.1.

——, L. Bard, L. Stoecker, and B. Geerts, 2018: Influence of Lake Erie on a Lake Ontario lake-effect snowstorm. *J. Appl. Meteor. Climatol.*, **57**, 2019–2033, https://doi.org/10.1175/JAMC-D-17-0349.1.

Laird, N. F., and D. A. R. Kristovich, 2002: Variations of sensible and latent heat fluxes from a Great Lakes buoy and associated synoptic weather patterns. *J. Hydrometeor.*, **3**, 3–12, https://doi.org/10.1175/1525-7541(2002)003<0003:VOSALH>2.0.CO;2.

——, and ——, 2004: Comparison of observations with idealized model results for a method to resolve winter lake-effect mesoscale morphology. *Mon. Wea. Rev.*, **132**, 1093–1103, https://doi.org/10.1175/1520-0493(2004)132<1093:COOWIM>2.0.CO;2.

——, ——, and J. E. Walsh, 2003: Model simulations examining the relationship of lake-effect morphology to lake shape, wind direction, and wind speed. *Mon. Wea. Rev.*, **131**, 2102–2111, https://doi.org/10.1175/1520-0493(2003)131<2102:MSETRO>2.0.CO;2.

Lang, C. E., J. M. McDonald, L. Gaudet, D. Doeblin, E. A. Jones, and N. F. Laird, 2018: The influence of a lake-to-lake Connection from Lake Huron on the lake-effect snowfall in the vicinity of Lake Ontario. *J. Appl. Meteor. Climatol.*, **57**, 1423–1439, https://doi.org/10.1175/JAMC-D-17-0225.1.

Langbein, W. B., and Coauthors, 1947: Major winter and nonwinter floods in selected basins in New York and Pennsylvania. USGS Water-Supply Paper 915, 139 pp., https://pubs.usgs.gov/wsp/0915/report.pdf.

Mass, C., N. Johnson, M. Warner, and R. Vargas, 2015: Synoptic control of cross-barrier precipitation ratios for the Cascade Mountains. *J. Hydrometeor.*, **16**, 1014–1028, https://doi.org/10.1175/JHM-D-14-0149.1.

May, R. M., and Coauthors, 2022: MetPy: A meteorological Python library for data analysis and visualization. *Bull. Amer. Meteor. Soc.*, **103**, E2273–E2284, https://doi.org/10.1175/BAMS-D-21-0125.1.

Minder, J. R., T. W. Letcher, L. S. Campbell, P. G. Veals, and W. J. Steenburgh, 2015: The evolution of lake-effect convection during landfall and orographic uplift as observed by profiling radars. *Mon. Wea. Rev.*, **143**, 4422–4442, https://doi.org/10.1175/MWR-D-15-0117.1.

Muller, R. A., 1966: Snowbelts of the Great Lakes. *Weatherwise*, **19**, 248–255, https://doi.org/10.1080/00431672.1966.10544204.

Nakai, S., and T. Endoh, 1995: Observation of snowfall and airflow over a low mountain barrier. *J. Meteor. Soc. Japan*, **73**, 183–199, https://doi.org/10.2151/jmsj1965.73.2_183.

National Weather Service, 2022: Northeast annual average snowfall. NOAA, accessed 5 November 2022, https://www.weather.gov/btv/winter.

Niziol, T. A., 1987: Operational forecasting of lake effect snowfall in western and central New York. *Wea. Forecasting*, **2**, 310–321, https://doi.org/10.1175/1520-0434(1987)002<0310:OFOLES>2.0.CO;2.

——, W. R. Snyder, and J. S. Waldstreicher, 1995: Winter weather forecasting throughout the eastern United States. Part IV: Lake effect snow. *Wea. Forecasting*, **10**, 61–77, https://doi.org/10.1175/1520-0434(1995)010<0061:WWFTTE>2.0.CO;2.

Norin, L., and G. Haase, 2012: Doppler weather radars and wind turbines. *Doppler Radar Observations—Weather Radar, Wind Profiler, Ionospheric Radar, and Other Advanced Applications*, J. Bech, Ed., InTechOpen, 333–354.

Norton, D. C., and S. J. Bolsenga, 1993: Spatiotemporal trends in lake effect and continental snowfall in the Laurentian Great Lakes, 1951–1980. *J. Climate*, **6**, 1943–1956, https://doi.org/10.1175/1520-0442(1993)006<1943:STILEA>2.0.CO;2.

Passarelli, R. E., Jr., and R. R. Braham Jr., 1981: The role of the winter land breeze in the formation of Great Lake snow storms. *Bull. Amer. Meteor. Soc.*, **62**, 482–491, https://doi.org/10.1175/1520-0477(1981)062<0482:TROTWL>2.0.CO;2.

Peace, R. L., and R. B. Sykes, 1966: Mesoscale study of a lake effect snowstorm. *Mon. Wea. Rev.*, **94**, 495–507, https://doi.org/10.1175/1520-0493(1966)094<0495:MSOALE>2.3.CO;2.

Pierre, A., S. Jutras, C. Smith, J. Kochendorfer, V. Fortin, and F. Anctil, 2019: Evaluation of catch efficiency transfer functions

for unshielded and single-Alter-shielded solid precipitation measurements. *J. Atmos. Oceanic Technol.*, **36**, 865–881, https://doi.org/10.1175/JTECH-D-18-0112.1.

Radar Operations Center, 2022: How rotating wind turbine blades impact the NEXRAD Doppler weather radar. NOAA/NWS, accessed 24 October 2022, https://www.roc.noaa.gov/WSR88D/WindFarm/TurbinesImpactOn.aspx?wid=dev.

Ralph, F. M., P. J. Neiman, D. E. Kingsmill, P. O. G. Persson, A. B. White, E. T. Strem, E. D. Andrews, and R. C. Antweiler, 2003: The impact of a prominent rain shadow on flooding in California's Santa Cruz Mountains: A CALJET case study and sensitivity to the ENSO cycle. *J. Hydrometeor.*, **4**, 1243–1264, https://doi.org/10.1175/1525-7541(2003)004<1243:TIOAPR>2.0.CO;2.

Rasmussen, R., and Coauthors, 2012: How well are we measuring snow: The NOAA/FAA/NCAR winter precipitation test bed. *Bull. Amer. Meteor. Soc.*, **93**, 811–829, https://doi.org/10.1175/BAMS-D-11-00052.1.

Reinking, R. F., and Coauthors, 1993: The Lake Ontario Winter Storms (LOWS) project. *Bull. Amer. Meteor. Soc.*, **74**, 1828–1850, https://doi.org/10.1175/1520-0477-74-10-1828.

Roe, G. H., and M. B. Baker, 2006: Microphysical and geometrical controls on the pattern of orographic precipitation. *J. Atmos. Sci.*, **63**, 861–880, https://doi.org/10.1175/JAS3619.1.

Rosenow, A. A., D. M. Plummer, R. M. Rauber, G. M. McFarquhar, B. F. Jewett, and D. Leon, 2014: Vertical velocity and physical structure of generating cells and convection in the comma head region of continental winter cyclones. *J. Atmos. Sci.*, **71**, 1538–1558, https://doi.org/10.1175/JAS-D-13-0249.1.

Schmidlin, T. W., 1993: Impacts of severe winter weather during December 1989 in the Lake Erie snowbelt. *J. Climate*, **6**, 759–767, https://doi.org/10.1175/1520-0442(1993)006<0759:IOSWWD>2.0.CO;2.

Siler, N., and D. Durran, 2016: What causes weak orographic rain shadows? Insights from case studies in the Cascades and idealized simulations. *J. Atmos. Sci.*, **73**, 4077–4099, https://doi.org/10.1175/JAS-D-15-0371.1.

——, G. Roe, and D. Durran, 2013: On the dynamical causes of variability in the rain-shadow effect: A case study of the Washington Cascades. *J. Hydrometeor.*, **14**, 122–139, https://doi.org/10.1175/JHM-D-12-045.1.

Sinclair, M. R., D. S. Wratt, R. D. Henderson, and W. R. Gray, 1997: Factors affecting the distribution and spillover of precipitation in the Southern Alps of New Zealand—A case study. *J. Appl. Meteor.*, **36**, 428–442, https://doi.org/10.1175/1520-0450(1997)036<0428:FATDAS>2.0.CO;2.

Steenburgh, J., 2023: *Secrets of the Greatest Snow on Earth*. 2nd ed. Utah State University Press, 213 pp.

Steenburgh, W. J., and L. S. Campbell, 2017: The OWLeS IOP2b lake-effect snowstorm: Shoreline geometry and the mesoscale forcing of precipitation. *Mon. Wea. Rev.*, **145**, 2421–2436, https://doi.org/10.1175/MWR-D-16-0460.1.

Steiger, S. M., R. Hamilton, J. Keeler, and R. E. Orville, 2009: Lake-effect thunderstorms in the lower Great Lakes. *J. Appl. Meteor. Climatol.*, **48**, 889–902, https://doi.org/10.1175/2008JAMC1935.1.

——, and Coauthors, 2013: Circulations, bounded weak echo regions, and horizontal vortices observed within long-lake-axis-parallel–lake-effect storms by the Doppler on wheels. *Mon. Wea. Rev.*, **141**, 2821–2840, https://doi.org/10.1175/MWR-D-12-00226.1.

Stockham, A. J., D. M. Schultz, J. G. Fairman Jr., and A. P. Draude, 2018: Quantifying the rain-shadow effect: Results from the Peak District, British Isles. *Bull. Amer. Meteor. Soc.*, **99**, 777–790, https://doi.org/10.1175/BAMS-D-17-0256.1.

Vasiloff, S., 2001: WSR-88D performance in northern Utah during the winter of 1998–1999. Part I: Adjustments to precipitation estimates. NOAA/Western Regional Tech. Attachment 01-03, 5 pp.

Veals, P. G., and W. J. Steenburgh, 2015: Climatological characteristics and orographic enhancement of lake-effect precipitation east of Lake Ontario and over the Tug Hill Plateau. *Mon. Wea. Rev.*, **143**, 3591–3609, https://doi.org/10.1175/MWR-D-15-0009.1.

——, ——, and L. S. Campbell, 2018: Factors affecting the inland and orographic enhancement of lake-effect precipitation over the Tug Hill Plateau. *Mon. Wea. Rev.*, **146**, 1745–1762, https://doi.org/10.1175/MWR-D-17-0385.1.

——, ——, S. Nakai, and S. Yamaguchi, 2019: Factors affecting the inland and orographic enhancement of sea-effect snowfall in the Hokuriku Region of Japan. *Mon. Wea. Rev.*, **147**, 3121–3143, https://doi.org/10.1175/MWR-D-19-0007.1.

——, ——, ——, and ——, 2020: Intrastorm variability of the inland and orographic enhancement of a sea-effect snowstorm in the Hokuriku Region of Japan. *Mon. Wea. Rev.*, **148**, 2527–2548, https://doi.org/10.1175/MWR-D-19-0390.1.

Veron, F., W. K. Melville, and L. Lenain, 2008: Wave-coherent air–sea heat flux. *J. Phys. Oceanogr.*, **38**, 788–802, https://doi.org/10.1175/2007JPO3682.1.

Villani, J. P., M. L. Jurewicz Sr., and K. Reinhold, 2017: Forecasting the inland extent of lake effect snow bands downwind of Lake Ontario. *J. Oper. Meteor.*, **5**, 53–70, https://doi.org/10.15191/nwajom.2017.0505.

Welsh, D., B. Geerts, and P. Bergmaier, 2014: An airborne profiling view of lake-effect snow circulations transitioning from an open water surface to moderate terrain. *16th Conf. on Mountain Meteorology*, San Diego, CA, Amer. Meteor. Soc., P49, https://ams.confex.com/ams/16MountMet/webprogram/Paper252060.html.

Zagrodnik, J. P., L. McMurdie, and R. Conrick, 2021: Microphysical enhancement processes within stratiform precipitation on the barrier and sub-barrier scale of the Olympic Mountains. *Mon. Wea. Rev.*, **149**, 503–520, https://doi.org/10.1175/MWR-D-20-0164.1.

Zängl, G., 2005: The impact of lee-side stratification on the spatial distribution of orographic precipitation. *Quart. J. Roy. Meteor. Soc.*, **131**, 1075–1091, https://doi.org/10.1256/qj.04.118.

Zaremba, T. J., and Coauthors, 2022: Vertical motions in orographic cloud systems over the Payette River basin. Part I: Recovery of vertical motions and their uncertainty from airborne Doppler radial velocity measurements. *J. Appl. Meteor. Climatol.*, **61**, 1707–1725, https://doi.org/10.1175/JAMC-D-21-0228.1.

Zrnić, D. S., V. M. Melnikov, and A. V. Ryzhkov, 2006: Correlation coefficients between horizontally and vertically polarized returns from ground clutter. *J. Atmos. Oceanic Technol.*, **23**, 381–394, https://doi.org/10.1175/JTECH1856.1.